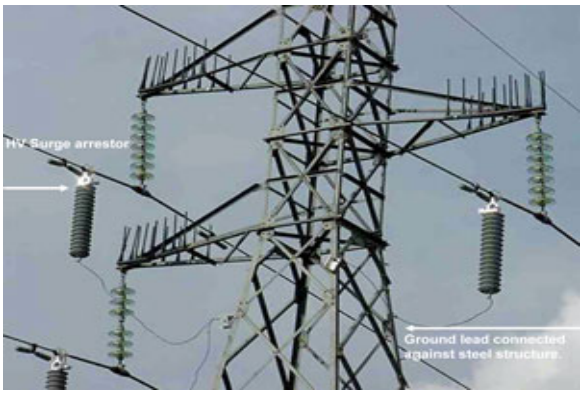

Chapter 6

Electrical and Structural Characterization of MnO Doped ZnO – V_2O_5 – Nb_2O_5 Varistor Ceramics Sintered at Different Temperatures.

Chapter 6

Electrical and Structural Characterization of MnO Doped ZnO – V_2O_5 – Nb_2O_5 Varistor Ceramics Sintered at Different Temperatures.

This chapter addresses the effect of MnO doping on electrical and strutural properties of ZnO–V_2O_5–Nb_2O_5 based varistors. The current chapter is divided into following two sections: -

Section 1: This section of the chapter describes synthesis of MnO doped ZnO–V_2O_5–Nb_2O_5 varistor ceramics sintered at 850 °C, 900 °C and 950 °C and their structural characterization using XRD, SEM and EDS.

Section 2: This section discusses the influence of the grain boundaries structure on the electrical properties of ZnO based ceramics in a systematic manner using AC impedance and dieclctric spectroscopy (IS). Various properties investigated include grain boundary resistance, dielectric constant (ε'), tan δ, non-linear coefficent, breakdown field, leakage current density and breakdown voltage per grain boundary.

Overview: The Nb doped ZnO–V_2O_5 varistor systems exhibits a low nonlinear coefficient. To improve the nonlinear properties and stability, MnO_2 and Mn_3O_4 doped ZnO–V_2O_5 varistor ceramics have been actively studied until now [Nahm et al. (2007, 2009, 2011 & 2015)]. However, MnO -doped ZnO–V_2O_5 varistor ceramics have been rarely studied. MnO has an advantage in terms of cost and availability when compared with MnO_2 and Mn_3O_4 [Nahm et al. (2007, 2009, 2011 & 2015)].

In chapter 5, we found that the electrical and dielectric properties of liquid-phase sintered ZnO–V_2O_5 ceramics doped with Nb_2O_5 critically depend on the grain boundary resistance using impedance spectroscopy (IS). Furthermore, Nb_2O_5-doped ZnO–V_2O_5 varistor ceramics have a nonlinear coefficient in the range of 4 to 7. Composition with 0.10 mol% Nb_2O_5 sintered at 900°C shows best

varistor characteristics among all the composition. To further improve the characteristics above composition i.e. 0.10 mol% Nb_2O_5 varistor system doped with MnO will be essential to be investigated. It is assumed that, the ZnO–V_2O_5–Nb_2O_5 ceramics doped with MnO will enhance the nonlinear properties. Therefore, it is necessary that MnO-doped ZnO–V_2O_5–Nb_2O_5 ceramics will be studied in detail in terms of grain boundary behaviour to tailor multi-layered chip varistors.

The present chapter further addresses the effect of MnO content on ZnO-V_2O_5-Nb_2O_5 based varistor systems sintered at 850 °C, 900 °C and 950 °C on the microstructure and the influence of the grain boundary structure on the electrical properties of ZnO based varistor ceramics in a systematic manner using AC impedance spectroscopy (IS).

6.1. Synthesis and Structural Behavior of MnO Doped ZnO – V_2O_5 – Nb_2O_5 Varistor ceramics.

Reagent grade high purity Sigma Aldrich: ZnO (> 99.00%), V_2O_5 (99.60%), Nb_2O_5 (99.99%) and MnO ($MnCO_3$) 99.90% were used as raw materials. To investigate the effect of MnO addition five compositions (99.4-x) mol% ZnO + 0.5 mol% V_2O_5 + 0.10 mol% Nb_2O_5 + x - mol% MnO (where x = 0.00, 1.50, 2.00, 2.50 and 3.00) were prepared using solid state reaction technique. The compositions chosen and the sintering conditions used for each varistor composition are summarized in Tables 6.1, 6.2 and 6.3. All the compositions were mixed homogeneously by conventional ball milling using zirconia balls in acetone in a poly-propylene bottle for 24 h. Thereafter, the mixtures were filtered, dried and calcined at 650 °C for 3 h. The agglomerates were pulverized using an agate mortar-pestle followed by uniaxially pressed into pellets having approximately diameters of 12 mm and thickness 1 mm in a hydraulic press at a pressure of 150 MPa using polyvinyl butyral (PVB) as a binder. The pellets were covered with raw powder and placed inside a closed double alumina crucible at different sintering temperature 850 °C, 900 °C and 950 °C respectively for a soaking period of 3 h with both heating and cooling rate of 3 °C/min. Before electrical measurements, the sintered pellets were polished with emery paper on both the sides and then annealed at 700 °C for 5 h to stabilize the electrical properties. High temperature conductive silver paste was used to coat both faces of the pellets and the electrodes were formed by curing the paste at 600 °C for 10 min.

A **nomenclature** e.g. 850NM150 is given to each sample. Here '850' denote the sintering temperature in °C, 'N' denotes Nb_2O_5, 'M' denotes MnO, '150' denotes the mole percent of MnO as 1.50 mol%. Tables 6.1, 6.2 and 6.3 shows the nomenclature of samples.

Table 6.1: Summary of samples composition and their nomenclature, sintered density 'ρ' and average grain size for samples sintered at 850 °C for 3 h.

Sample nomenclature	Composition: (Sintered at 850 °C for 3 h)				Sintered density (gm/cc)	Average grain size (μm)
	ZnO (mol%)	V_2O_5 (mol%)	Nb_2O_5 (mol%)	MnO (mol%)		
850NM000	99.40	0.50	0.10	0.00	5.32	5.3
850NM150	97.90	0.50	0.10	1.50	5.37	5.7
850NM200	97.40	0.50	0.10	2.00	5.37	5.5
850NM250	96.90	0.50	0.10	2.50	5.39	5.4
850NM300	96.40	0.50	0.10	3.00	5.38	5.2

Table 6.2: Summary of samples composition and their nomenclature, sintered density 'ρ' and average grain size for samples sintered at 900 °C for 3 h.

Sample nomenclature	Composition: (Sintered at 900 °C for 3 h)				Sintered density (gm/cc)	Average grain size (μm)
	ZnO (mol%)	V_2O_5 (mol%)	Nb_2O_5 (mol%)	MnO (mol%)		
900NM000	99.40	0.50	0.10	0.00	5.44	7.0
900NM150	97.90	0.50	0.10	1.50	5.44	7.8
900NM200	97.40	0.50	0.10	2.00	5.45	9.2
900NM250	96.90	0.50	0.10	2.50	5.46	8.4
900NM300	96.40	0.50	0.10	3.00	5.48	9.3

Table 6.3: Summary of samples composition and their nomenclature, sintered density 'ρ' and average grain size for samples sintered at 950 °C for 3 h.

Sample nomenclature	Composition: (Sintered at 950 °C for 3 h)				Sintered density (gm/cc)	Average grain size (μm)
	ZnO (mol%)	V_2O_5 (mol%)	Nb_2O_5 (mol%)	MnO (mol%)		
950NM000	99.40	0.50	0.10	0.00	5.43	10.110
950NM150	97.90	0.50	0.10	1.50	5.46	16.161
950NM200	97.40	0.50	0.10	2.00	5.47	16.782
950NM250	96.90	0.50	0.10	2.50	5.49	15.875
950NM300	96.40	0.50	0.10	3.00	5.48	18.534

6.1.1. X-Ray Diffraction (XRD)

The strong and sharp diffraction peaks of the XRD patterns of ZnO varistors sintered at temperature 850 °C, 900 °C and 950 °C are shown in Figs. 6.1, 6.2 and 6.3 respectively and demonstrate that the products are well crystalline. Diffraction peaks present in the XRD patterns of different specimens were matched with the XRD - JCPDS files of constituent phases and other compounds which might have formed during sintering. It has been found that peaks in the XRD patterns matched with JCPDS files of hexagonal ZnO (file no. 361451). Crystallite size of different phases was calculated from the measurement of FWHM of XRD peaks of different phases using Scherer formula. From the calculated values, it can be found that the crystallite size lies in the range of 53-59 nm.

Fig. 6.1 shows XRD patterns of the samples 850NM000, 850NM150, 850NM200, 850NM250 and 850NM300 sintered at 850 °C for 3 h. For all of the samples doped with MnO, Apart from the major ZnO phase, $Zn_3(VO_4)_2$ (JCPDS card no. 191470, 191468 and 340378) and ZnV_2O_4 (JCPDS card no. 750318) were detected as minor secondary phases formed at the grain boundaries and the triple point junction. The secondary phases were produced by the following chemical reaction: $3ZnO + V_2O_5 \rightarrow Zn_3(VO_4)_2$.The major peaks could be indexed as reflections from planes (100), (002), (101), (102) and (110) of hexagonal ZnO. These were identified by comparing with standard JCPDS card no. 361451.The lattice parameters and the crystallite size for MnO-doped ZnO varistor samples sintered at 850 °C is given in Table 6.4. The larger lattice parameters of MnO-doped samples are due to the larger radii of Mn^{2+} (0.080 nm). With a radius greater than that of Zn^{2+} ion (0.074 nm), Mn^{2+} ions enter into the ZnO lattice, occupy the sites of Zn^{2+} ions and cause an expansion in the lattice parameter, and it is thought that Mn ions substitute for Zn ions. The peak positions of (002) for 0.00, 1.50, 2.00, 2.50, 3.00 mol% MnO-doped ZnO–V_2O_5–Nb_2O_5 samples sintered at 850 ºC are 34.46, 34.47, 34.48, 34.48, 34.42 degree respectively (Table: 6.4). It can be observed from the data that with Mn doping the peak positions of (002) planes shift slightly toward higher angle as compared to un-doped Mn sample.

The crystallite size for 0.00, 1.50, 2.00, 2.50 and 3.00 mol% MnO-doped ZnO–V_2O_5–Nb_2O_5 samples sintered at 850 °C are obtained as 53.9, 54.7, 57.9, 58.0 and 59.3 nm respectively are given in Table 6.4.

Table 6.4: Lattice parameters, percentage theoretical density (T.D) and crystallite size D (nm) MnO doped ZnO-V_2O_5-Nb_2O_5 varistor sintered at 850 °C.

Sample name	a = b (A°)	c (A°)	Unit cell volume ($A°^3$)	Percentage theoretical density (T.D)	Crystallite size for (002) D (nm)	2θ° for (002)
850NM000	3.248	5.203	47.556	93.55	53.9	34.462
850NM150	3.249	5.203	47.577	94.47	54.7	34.477
850NM200	3.248	5.202	47.554	94.55	57.9	34.479
850NM250	3.249	5.203	47.571	94.83	58.0	34.478
850NM300	3.250	5.205	47.645	94.88	59.3	34.424

X-ray diffraction patterns of 0.00, 1.50, 2.00, 2.50 and 3.00 mol% MnO-doped ZnO–V_2O_5–Nb_2O_5 samples sintered at 900 °C for 3 h are shown in Fig. 6.2. . For all of the samples doped with MnO, Apart from the major ZnO phase, $Zn_3(VO_4)_2$ (JCPDS card no. 191470, 191468 and 340378) and ZnV_2O_4(JCPDS card no. 750318) were detected as minor secondary phases formed at the grain boundaries and the triple point junction. The major peaks could be indexed as reflections from the planes (100), (002), (101), (102) and (110) of hexagonal ZnO. These were identified by comparing with standard JCPDS card no. 361451.The lattice parameters and the crystallite size D (nm) for the (002) of the MnO -doped ZnO varistor samples sintered at temperature 900 °C is summerised in Table 6.5.

Table 6.5: Lattice parameters, percentage theoretical density (T.D) & crystallite size D (nm) for MnO doped ZnO-V_2O_5-Nb_2O_5 varistor sintered at 900 °C

Sample name	a = b (A°)	c (A°)	Unit cell volume ($A°^3$)	Percentage theoretical density (T.D)	Crystallite size for (002) D (nm)	2θ° for (002)
900NM000	3.245	5.193	47.355	95.25	59.5	34.562
900NM150	3.250	5.207	47.629	95.99	57.1	34.458
900NM200	3.251	5.207	47.658	96.13	58.0	34.418
900NM250	3.254	5.209	47.765	96.41	54.1	34.465
900NM300	3.249	5.203	47.563	96.45	59.2	34.463

The peak positions of (002) for 0.00, 1.50, 2.00, 2.50, 3.00 mol% MnO-doped ZnO–V_2O_5–Nb_2O_5 samples sintered at 900 °C are 34.56, 34.46, 34.42, 34.46, 34.46 degree respectively (Table: 6.5). It can be observed from the data that with Mn doping the peak positions of (002) planes shift slightly toward lower angle as compared with un-doped Mn sample.

The crystallite size of (002) for 0.00, 1.50, 2.00, 2.50 and 3.00 mol% MnO-doped ZnO–V_2O_5–Nb_2O_5 samples sintered at 900 °C is obtained as 59.5, 57.1, 58.0, 54.1and 59.2 respectively are given in Table 6.5.

Fig. 6.3 shows XRD patterns of 0.0, 1.5, 2.0, 2.5 and 3.0 mol% MnO-doped ZnO–V_2O_5–Nb_2O_5 samples sintered at 950 °C for 3 hrs. For all of the samples doped with MnO, other than the major ZnO phase, $Zn_3(VO_4)_2$ (JCPDS card no. 191470, 191468 and 340378) and ZnV_2O_4 (JCPDS card no. 750318) were detected as minor secondary phases. The secondary phases were produced by the following chemical reaction: $3ZnO+V_2O_5 \rightarrow Zn_3(VO_4)_2$.The major peaks could be indexed as reflections from planes (100), (002), (101), (102) and (110) of hexagonal ZnO. These were identified by comparing with standard JCPDS card no. 361451.The lattice parameters and the crystallite size D (nm) for the (002) of the MnO doped ZnO varistor samples sintered at temperature 950 °C is given in Table 6.6. The peak positions of (002) plane for 0.00, 1.50, 2.00, 2.50 and 3.00 mol% MnO doped ZnO–V_2O_5–Nb_2O_5 samples sintered at 950 °C are 34.44, 34.45, 34.44,

34.45, 34.40 degree respectively (Table: 6.6). It can be observed from the data that with Mn-doping the peak positions of (002) planes shift slightly toward lower angle compared to un-doped Mn ZnO specimen. The crystallite size of (002) for 0.00, 1.50, 2.00, 2.50 and 3.00 mol% MnO-doped ZnO–V_2O_5–Nb_2O_5 samples sintered at 950 °C are obtained as 60.0, 55.6, 56.7, 57.3 and 57.7 nm respectively are given in Table 6.6

Table 6.6: Lattice parameters, percentage theoretical density (T.D) & crystallite size D (nm) for MnO doped ZnO-V_2O_5-Nb_2O_5 varistor sintered at 950 °C

Sample name	a = b (A°)	c (A°)	Unit cell volume ($A°^3$)	Percentage theoretical density (T.D)	Crystallite size for (002) D (nm)	2θ° for (002)
950NM000	3.249	5.206	47.590	95.59	60.0	34.445
950NM150	3.251	5.208	47.674	96.27	55.6	34.451
950NM200	3.249	5.204	47.591	96.32	56.7	34.440
950NM250	3.249	5.203	47.575	96.61	57.3	34.447
950NM300	3.250	5.208	47.656	96.67	57.7	34.458

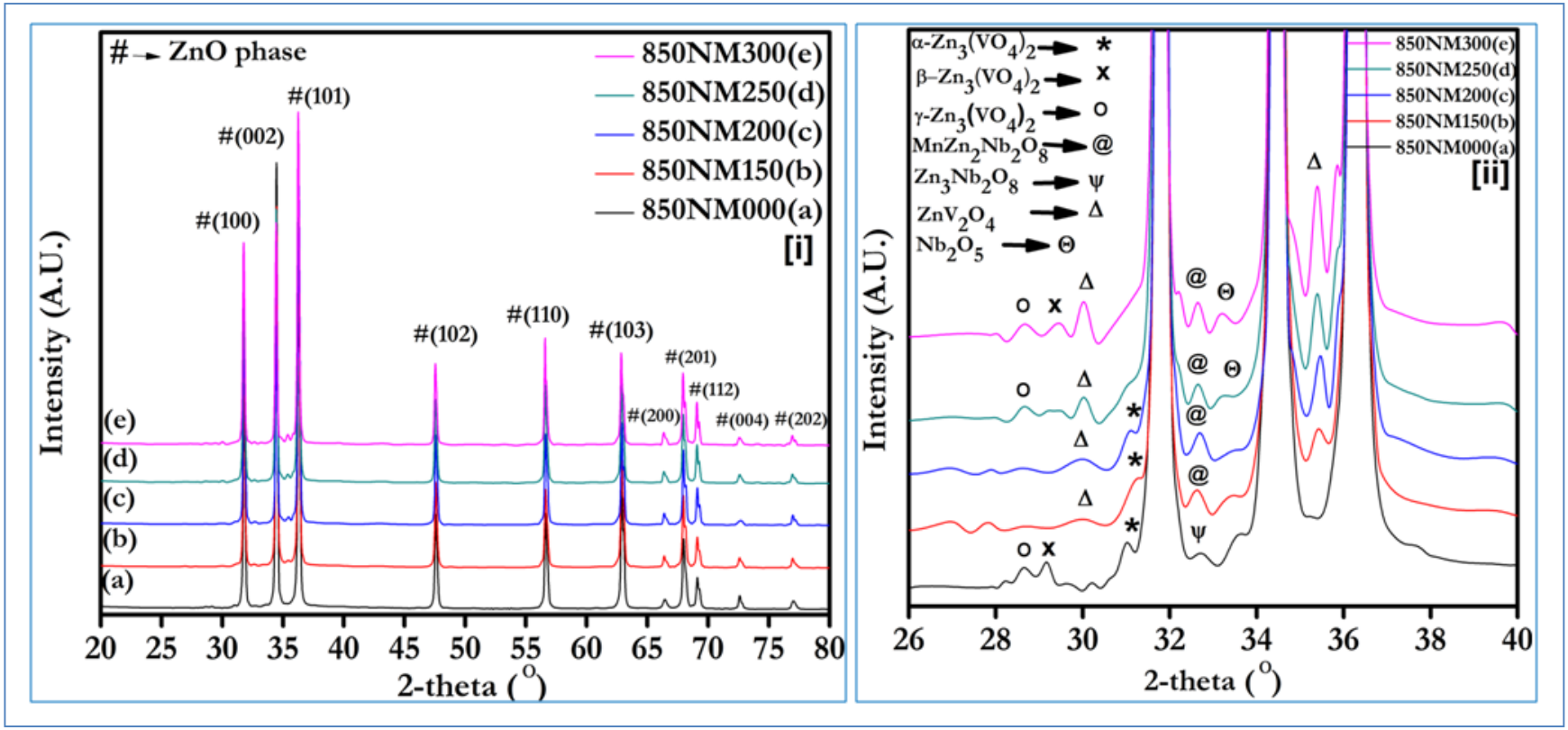

Figure 6.1: X-ray diffraction patterns of samples sintered at 850ºC with following compositions: (a) 850NM000 (0.00 mol% MnO); (b) 850NM150 (1.50 mol% MnO); (c) 850NM200 (2.00 mol% MnO); (d) 850NM250 (2.50 mol% MnO) and (e) 850NM300 (3.00 mol% MnO)

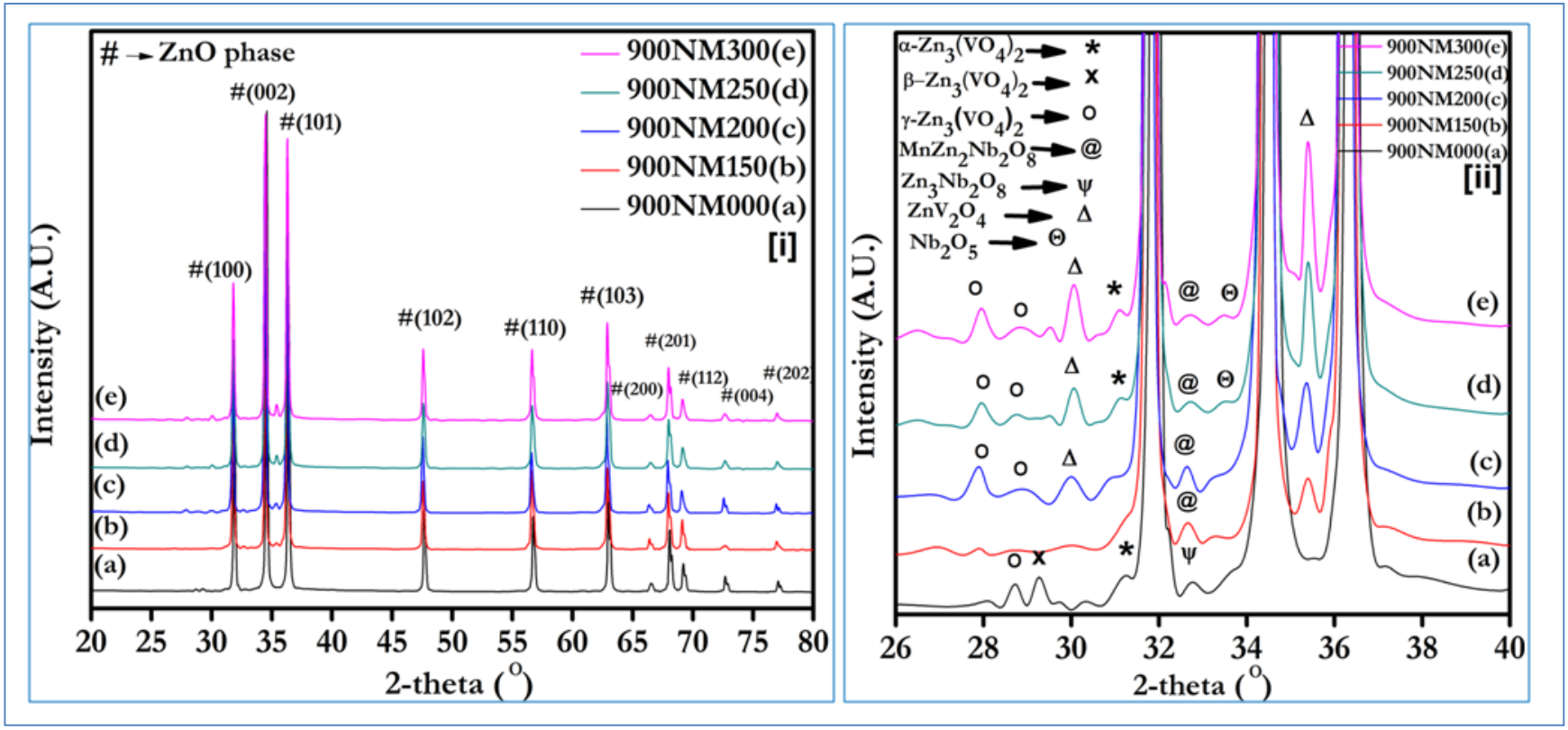

Figure 6.2: X-ray diffraction patterns of samples sintered at 900ºC with following compositions: (a) 900NM000 (0.00 mol% MnO); (b) 900NM150 (1.50 mol% MnO); (c) 900NM200 (2.00 mol% MnO); (d) 900NM250 (2.50 mol% MnO) and (e) 900NM300 (3.00 mol% MnO)

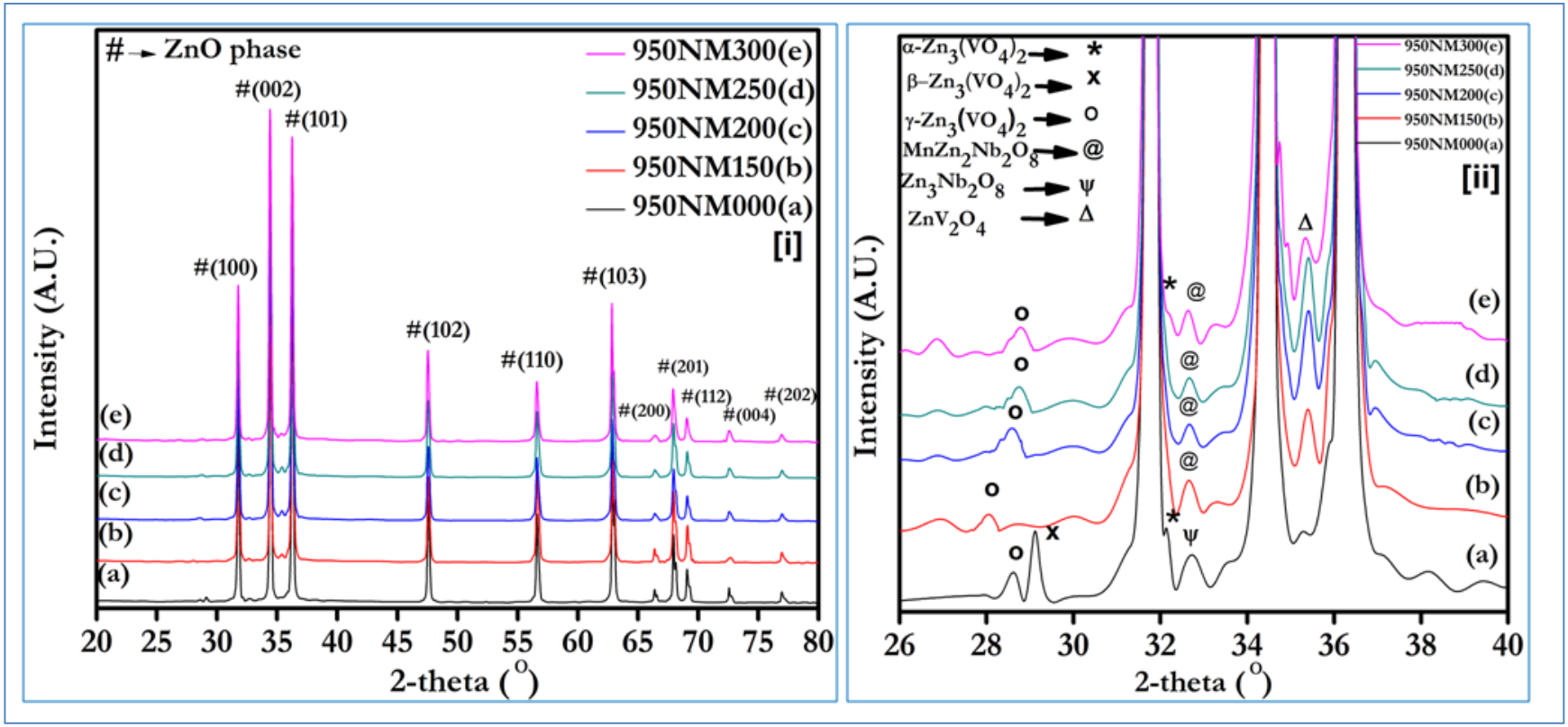

Figure 6.3: X-ray diffraction patterns of samples sintered at 950ºC with following compositions: (a) 950NM000 (0.00 mol% MnO); (b) 950NM150 (1.50 mol% MnO); (c) 950NM200 (2.00 mol% MnO); (d) 950NM250 (2.50 mol% MnO) and (e) 950NM300 (3.00 mol% MnO)

6.1.2. Scanning Electron Microscopy (SEM)

Figs. 6.4 shows the SEM micrographs of the thermally etched samples sintered at 850 °C for 0.00, 1.50, 2.00, 2.50 and 3.00 mol% MnO-doped ZnO–V_2O_5–Nb_2O_5 samples at 10000X magnification (or 10 μm scale). Grain size are calculated as 5.3, 5.7, 5.5, 5.4 and 5.2 μm respectively from SEM micrographs. Small, closely spaced anhedral grains were nonuniformly distributed across the sample. Since the eutectic temperature for V_2O_5–ZnO is approximately 600°C, a liquid phase sintering process occurs when the sintering temperature is higher than the eutectic temperature that's lead to grain growth of ZnO and to densification of sample. For the samples sintered at 850 °C, the overall trend in the grain growth increases and then decreases with increase of MnO doping concentration. This indicates that MnO acts as a grain growth enhancer. The sample microstructure shown in Figs. 6.4 (a–e) was quite dense, with areas of closed spherical porosity, indicating the sintering process had reached to the final stage. Anisotropic grain growth results from sintering in the presence of a liquid phase. Overall, it can be seen that the grain size is inhomogeneous, despite clear grain boundaries. The average grain size of the 0.00 mol% MnO system was found to be 5.2 μm, which increased to 5.765 μm by addition of 1.50 mol% MnO. Further addition of MnO decreased the average grain size to 5.2 μm. The sample doped with 2.00 mol% MnO exhibited the most uniform grain size of 5.5 μm.

Figs. 6.5 shows the SEM micrographs of the thermally etched samples sintered at 900 °C for 0.00, 1.50, 2.00, 2.50 and 3.00 mol% MnO doped ZnO–V_2O_5–Nb_2O_5 samples at 5000X magnification (or 30 μm scale). Grain size of 7.0, 7.8, 9.2, 8.4 and 9.3 μm respectively are caculated from SEM micrographs. Microstructures at low magnification show a dense phase micrograph with small amount of porosity indicating that the sintering process had reached the final stage. Anisotropic grain growth observed resulting from sintering in the presence of a liquid phase. For the samples sintered at 900°C, the average grain size of the 0.00 mol% MnO system was found to be 7.0 μm, which first incresed to 9.2 μm by addition of 2.00 mol% MnO. Further addition of MnO (2.5 mol %) decreased the average grain size abnormally to 8.4 μm. The ZnO–V_2O_5–Nb_2O_5 doped with 2.5 mol% MnO exhibited the most uniform grain size.

SEM micrographs of the thermally etched samples sintered at 950 °C for 0.0, 1.5, 2.0, 2.5 and 3.0 mol% MnO-doped ZnO–V_2O_5–Nb_2O_5 samples at 5000X magnification (or 30 μm scale) are shown in Figs. 6.6. Grain size are calculated as 10.1, 16.2, 16.7, 15.9 and 18.5 μm respectively from SEM micrograph. Microstructures at low magnification show a dense phase micrograph with areas of the closed spherical porosity indicating that the sintering process had reached to the final stage. Anisotropic grain growth obsered resulting from sintering in the presence of a liquid phase. For the samples sintered at 950 °C. The average grain size of the 0.0 mol% MnO system was found to be 10.1 μm, which first incresed to 16.2 μm by addition of 1.5 mol% MnO. Further addition of MnO (2.0 mol %) increased the average grain size to 16.7 μm. The specimen with 3.00 mol% MnO exhibited the largest grain size of 18.5 μm among all the samples. The microstructure observation revealed that the MnO acts as a grain growth enhancer. For 1.5 mol% MnO sample, MnO could precipitate with ZnO along the grain boundaries and participates in lowering the grain size of the Mn-doped samples.

SEM micrographs of the samples at different MnO content show the following features: (i) the average grain size depends on the MnO doping, (ii) there were large grains dispersed in a matrix composed of small grains, (iii) the large grains grew faster than the small grains, (iv) the large grains always had an oblong shape and (v) the microstructure observation revealed that the MnO acts as a grain growth enhancer. With respect to the oblong shape of exaggerated grains, it observed that the grain growth in these samples was quite anisotropic.

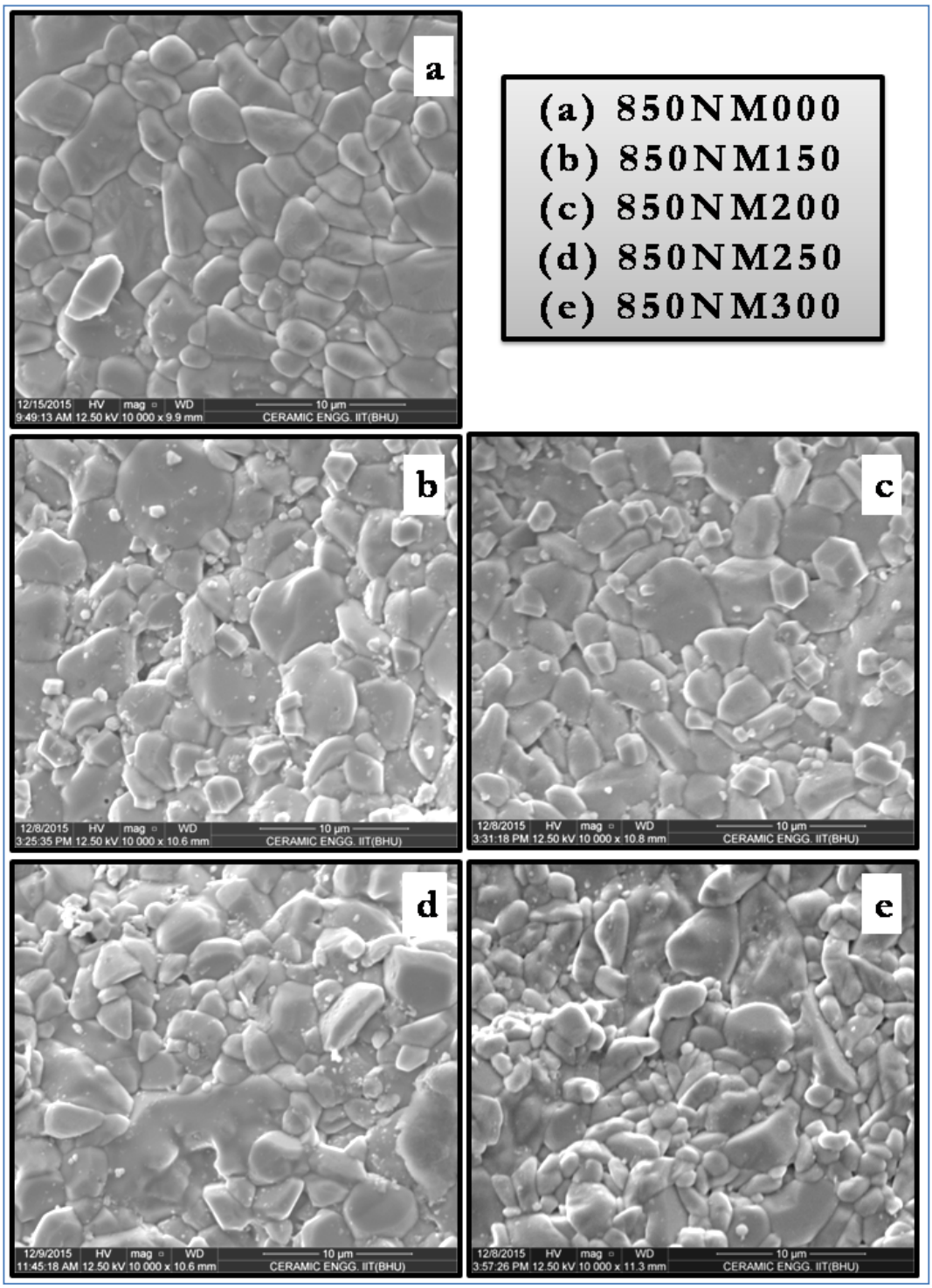

Figure 6.4: SEM micrographs of the sample sintered at 850 °C with following compositions: (a) 850NM000 (0.00 mol% MnO); (b) 850NM150 (1.50 mol% MnO); (c) 850NM200 (2.00 mol% MnO); (d) 850NM250 (2.50 mol% MnO); and (e) 850NM300 (3.00 mol% MnO)

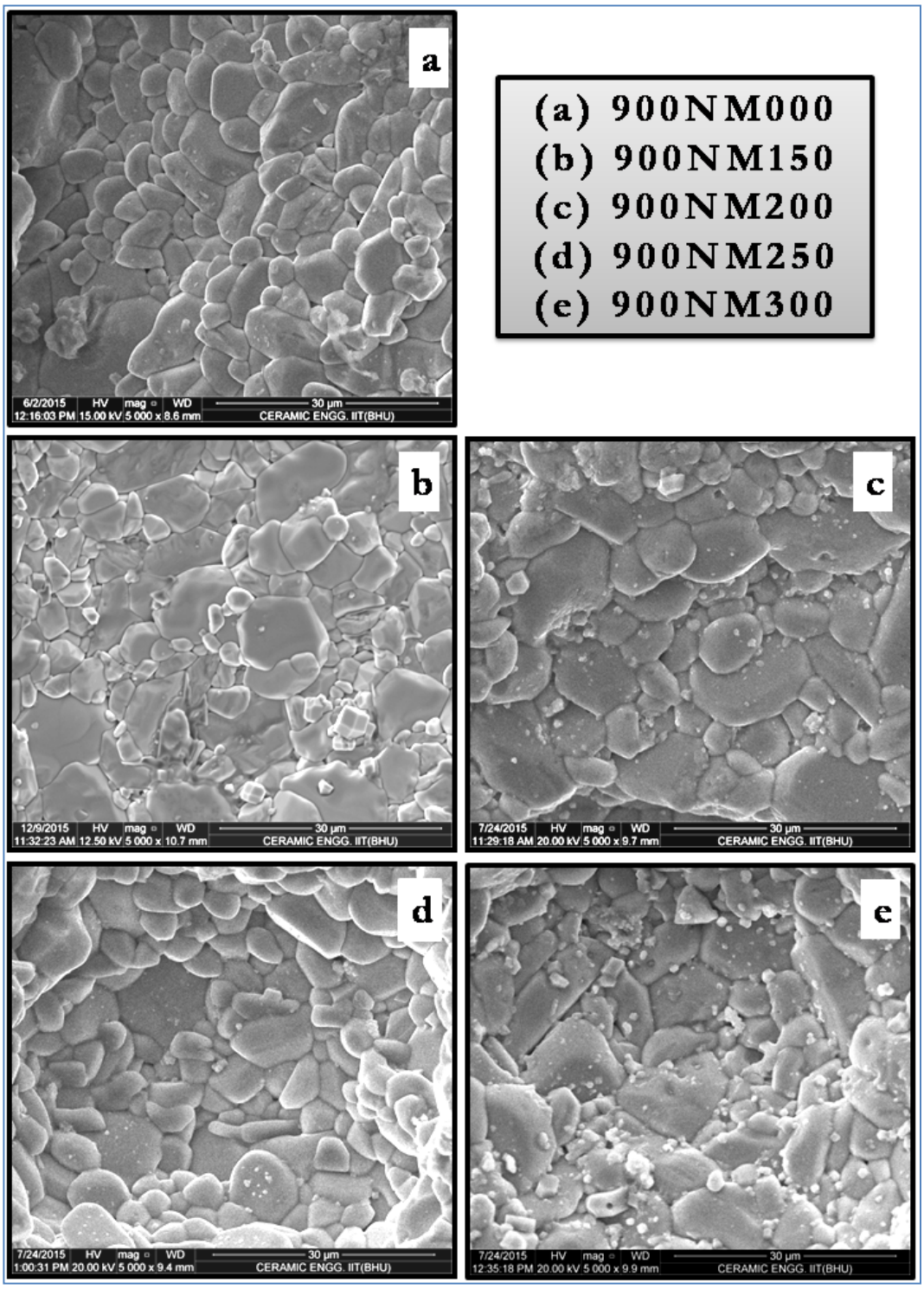

Figure 6.5: SEM micrographs of the sample sintered at 900 °C with following compositions: (a) 900NM000 (0.00 mol% MnO); (b) 900NM150 (1.50 mol% MnO); (c) 900NM200 (2.00 mol% MnO); (d) 900NM250 (2.50 mol% MnO); and (e) 900NM300 (3.00 mol% MnO)

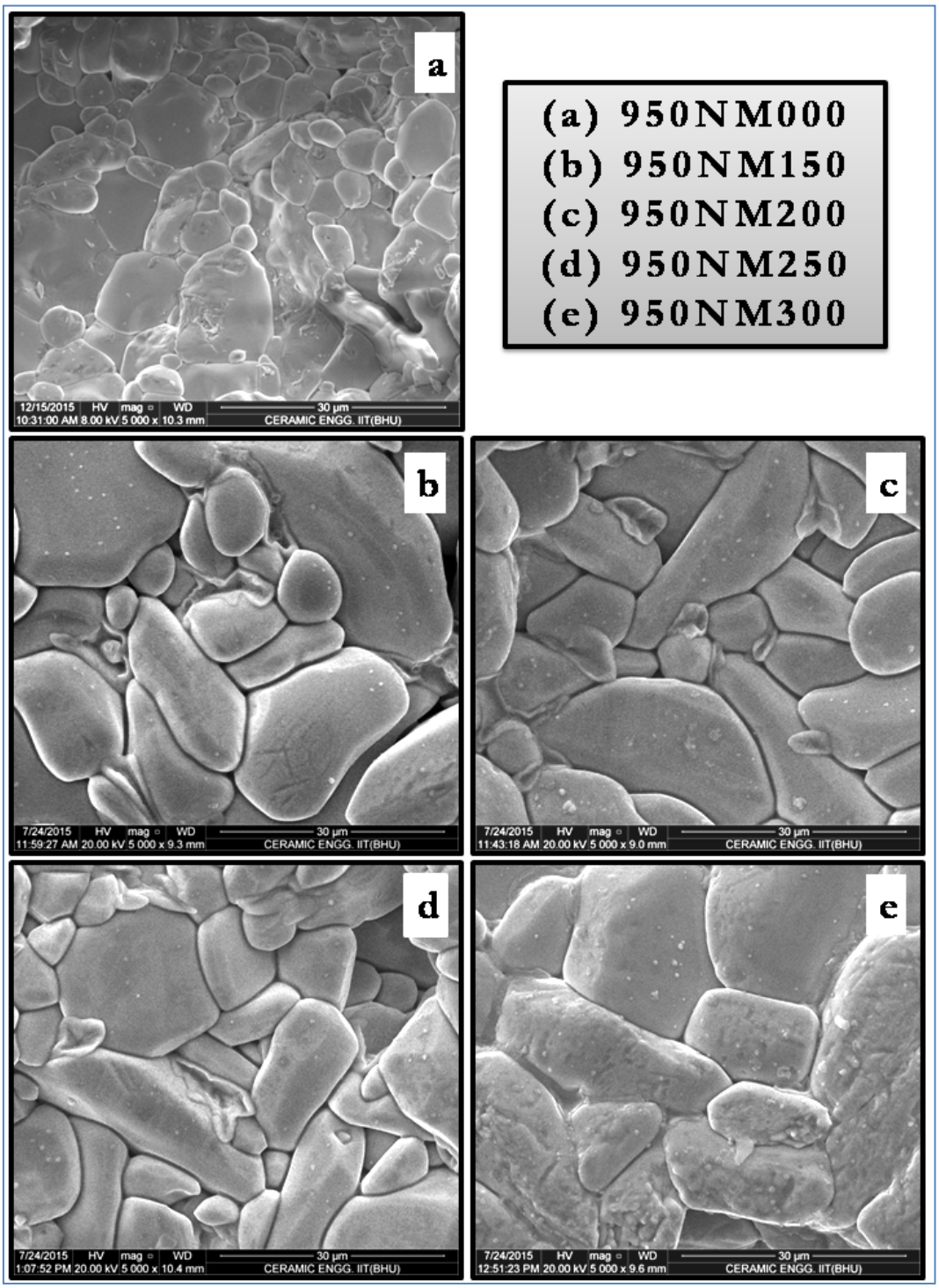

Figure 6.6: SEM micrographs of the sample sintered at 950 °C with following compositions: (a) 950NM000 (0.00 mol% MnO); (b) 950NM150 (1.50 mol% MnO); (c) 950NM200 (2.00 mol% MnO); (d) 950NM250 (2.50 mol% MnO); and (e) 950NM300 (3.00 mol% MnO)

6.1.3. Energy-Dispersive X-ray Spectroscopy (EDS)

EDS spectra for 2.00 mol% MnO sample (900NM200) at different regions, especially grain interiors and grain boundaries, are shown in Fig. 6.7. EDS spectra of the ZnO grain boundary reveal V, Nb and Mn segregation in the sample 900NM200. At triplet point, a secondary phase consists of Mn was confirmed by XRD and EDS spectra. Fig. 6.8 shows EDS elemental maps for Zn, O, V, Nb and Mn of samples with addition of 2.00 mol% MnO, 0.10 mol% Nb_2O_5, 0.50 mol% V_2O_5 and 97.40 mol% ZnO.

EDS spectra for 2.50 mol% MnO doped ZnO-V_2O_5-Nb_2O_5 (900NM250) sample sintered at 900°C at different regions, especially the grain interior and the grain boundary, are shown in Fig. 6.9 EDS spectra of the ZnO grain boundary shows V, Nb and Mn segregation in the sample (900NM250). At lower concentration, MnO could precipitate together with ZnO along the grain boundaries and participates in lowering the grain size of the doped samples. Fig. 6.10 shows EDS elemental maps for Zn, O, V, Nb and Mn of samples with the addition of 2.50 mol% MnO, 0.10 mol% Nb_2O_5, 0.50 mol%V_2O_5 and 96.90 mol% ZnO.

EDS spectra for 2.50 mol% MnO Doped ZnO-V_2O_5-Nb_2O_5 (950NM250) sample sintered at 950°C at different regions, especially the grain interior and the grain boundary, are shown in Fig. 6.11. EDS spectra of the ZnO grain boundary shows V, Nb and Mn segregation in sample (950NM250). This is due to the Mn^{2+} ions (0.80Å), which have larger ionic radius compare to Zn^{2+} (0.74Å) segregated at the grain boundaries as secondary. Fig. 6.12 shows EDS elemental maps for Zn, O, V, Nb and Mn of the samples with the addition of 2.50 mol% MnO, 0.10 mol% Nb_2O_5, 0.50 mol% V_2O_5 and 96.90 mol% ZnO.

EDS spectra for sample 950NM300 at different regions, especially grain interiors and grain boundaries, are shown in Fig. 6.13. EDS spectra of the ZnO grain boundary reveal V, Nb and Mn segregation in sample 950NM300. Fig. 6.14 shows EDS elemental maps for Zn, O, V, Nb and Mn of samples with the addition of 3.00 mol% MnO, 0.10 mol% Nb_2O_5, 0.50 mol% V_2O_5 and 96.40 mol% ZnO.

The grey-scale density in the EDS elemental maps images increases with increasing amount of an element present. V is present at the grain boundaries and coexists with segregated particles, such as spinel particles ZnV_2O_4 and the unknown compound at the triple points in the samples. The XRD and EDS analysis results reveal that V is incorporated in spinel particles.

EDS confirms that only Zn, O, Nb and Mn are present in the samples. The mass % of Zn and O in each sample was not as per stoichiometric proportion. The entire samples were observed to be oxygen deficient. The sample doped with 2.50 mol% MnO Doped ZnO-V_2O_5-Nb_2O_5 (950NM250) sample sintered at 950°C was observed to be most oxygen deficient. The deficiency or excess of the constituent material results in distorted band structure with corresponding decrease in resistivity. Zinc oxide loses oxygen on heating so that the zinc is in excess. The oxygen of course evolves as electrically neutral substance so that it is associated with each excess zinc ion in the crystal; there will be two electrons that remain trapped in the solid material, thus leading to non-stoichiometricity in the solid. This leads to the formation of the semiconducting nature of the material.

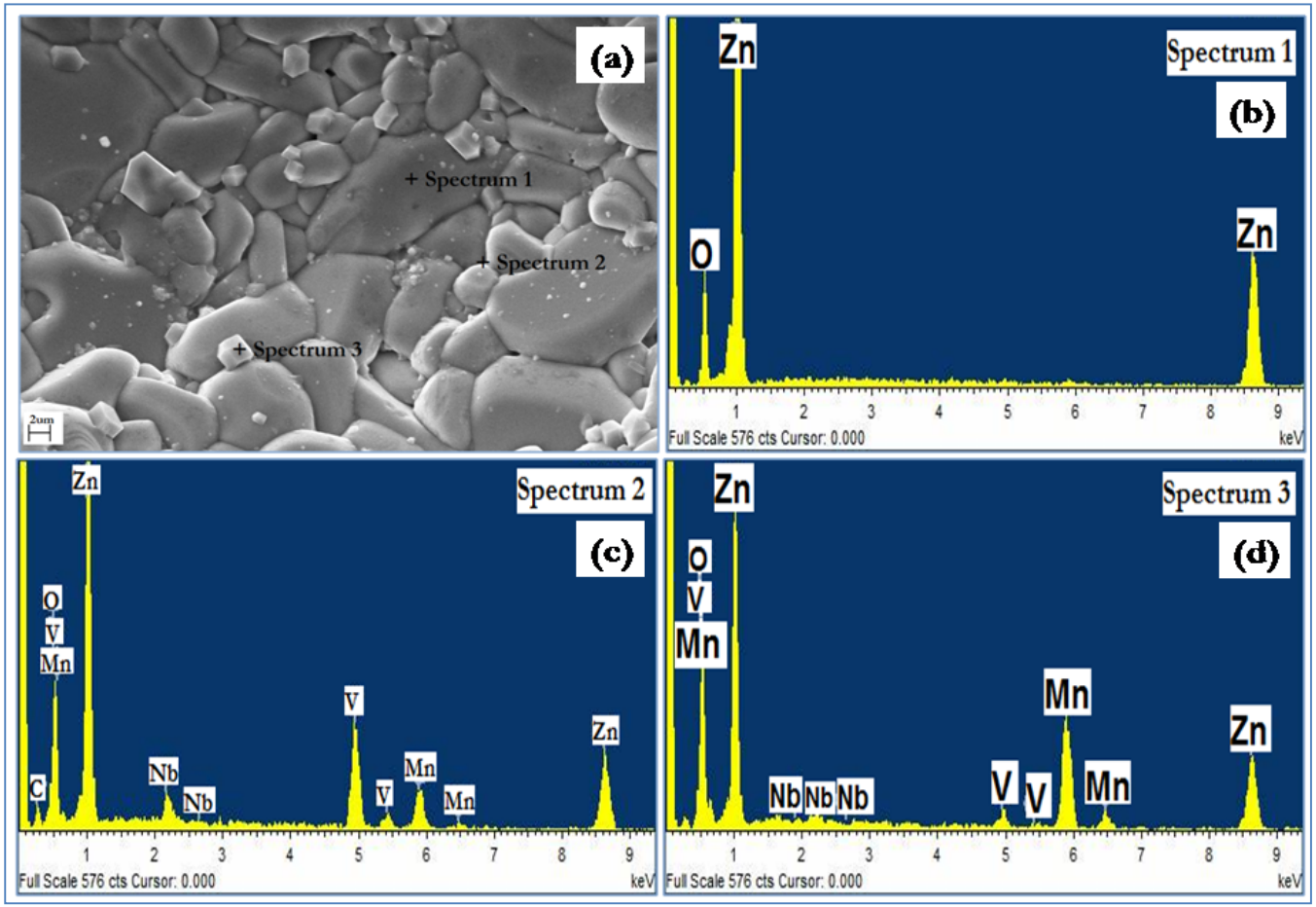

Figure 6.7: EDS spectra of 2.00mol% MnO Doped ZnO-V_2O_5-Nb_2O_5 System (900NM200) sintered at 900 °C: (a) SEM micrograph (b) at the ZnO grain (c) at the ZnO grain boundary showing V, Nb and Mn segregation in it and (d) at the selected region.

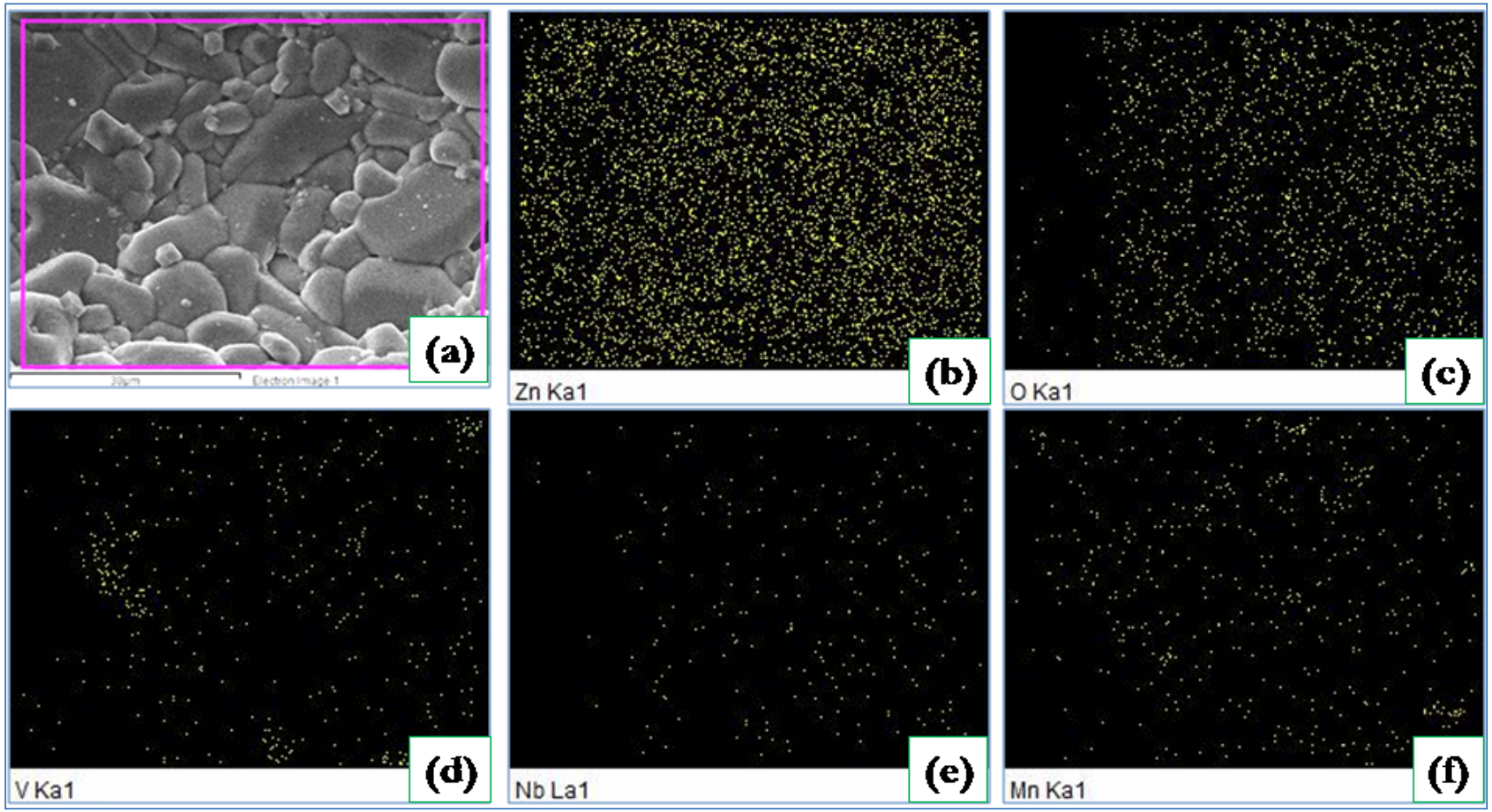

Figure 6.8: EDS elemental maps for 2.00 mol% MnO Doped ZnO-V_2O_5-Nb_2O_5 System (900NM200) sintered at 900 °C: (a) SEM micrograph (b) Zn map (c) O map (d) V map (e) Nb map and (f) Mn map

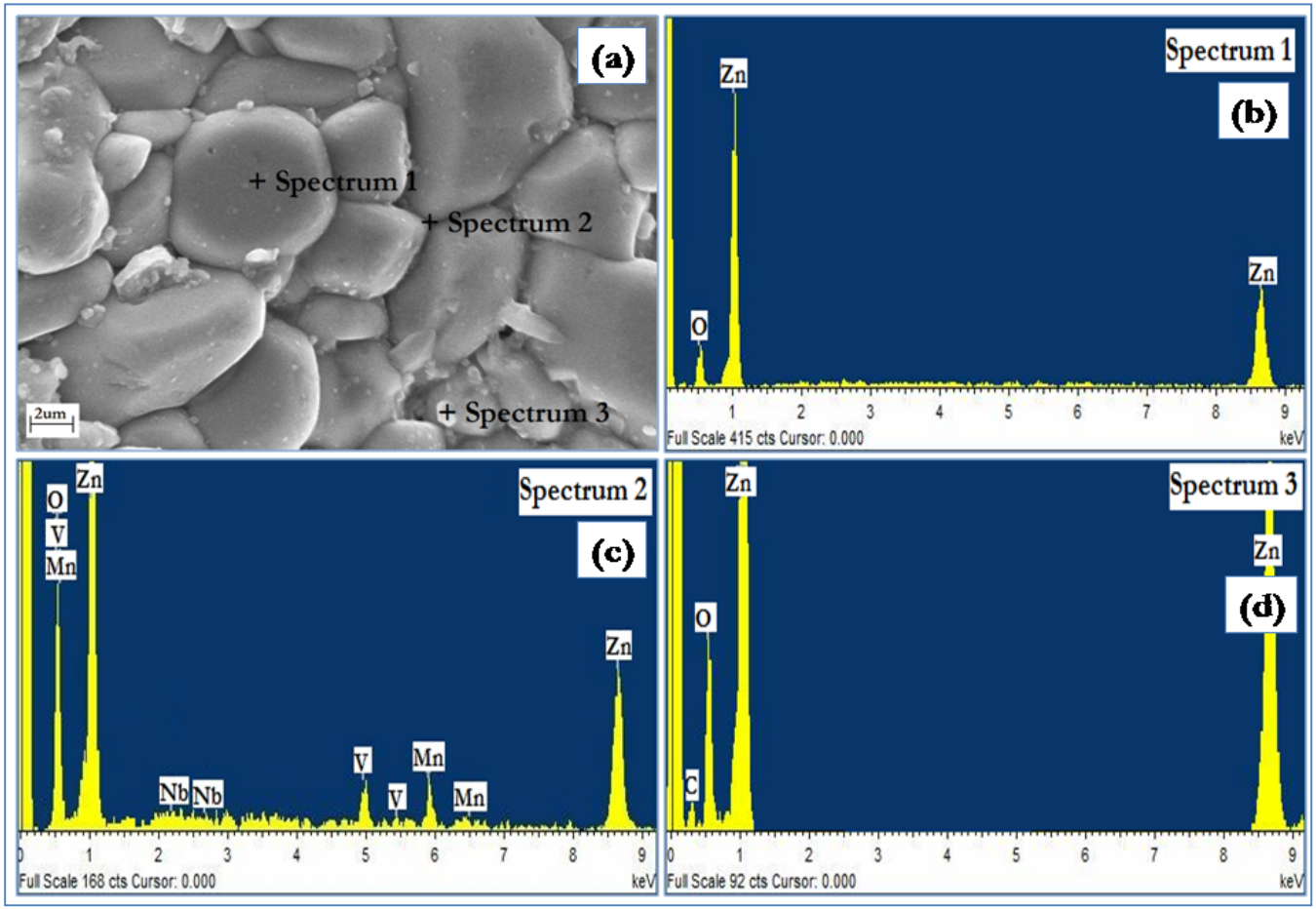

Figure 6.9: EDS spectra of 2.50 mol% MnO Doped ZnO-V_2O_5-Nb_2O_5 System (900NM250) sintered at 900 °C: (a) SEM micrograph (b) at the ZnO grain (c) at the ZnO grain boundary showing V, Nb and Mn segregation in it and (d) at the selected region.

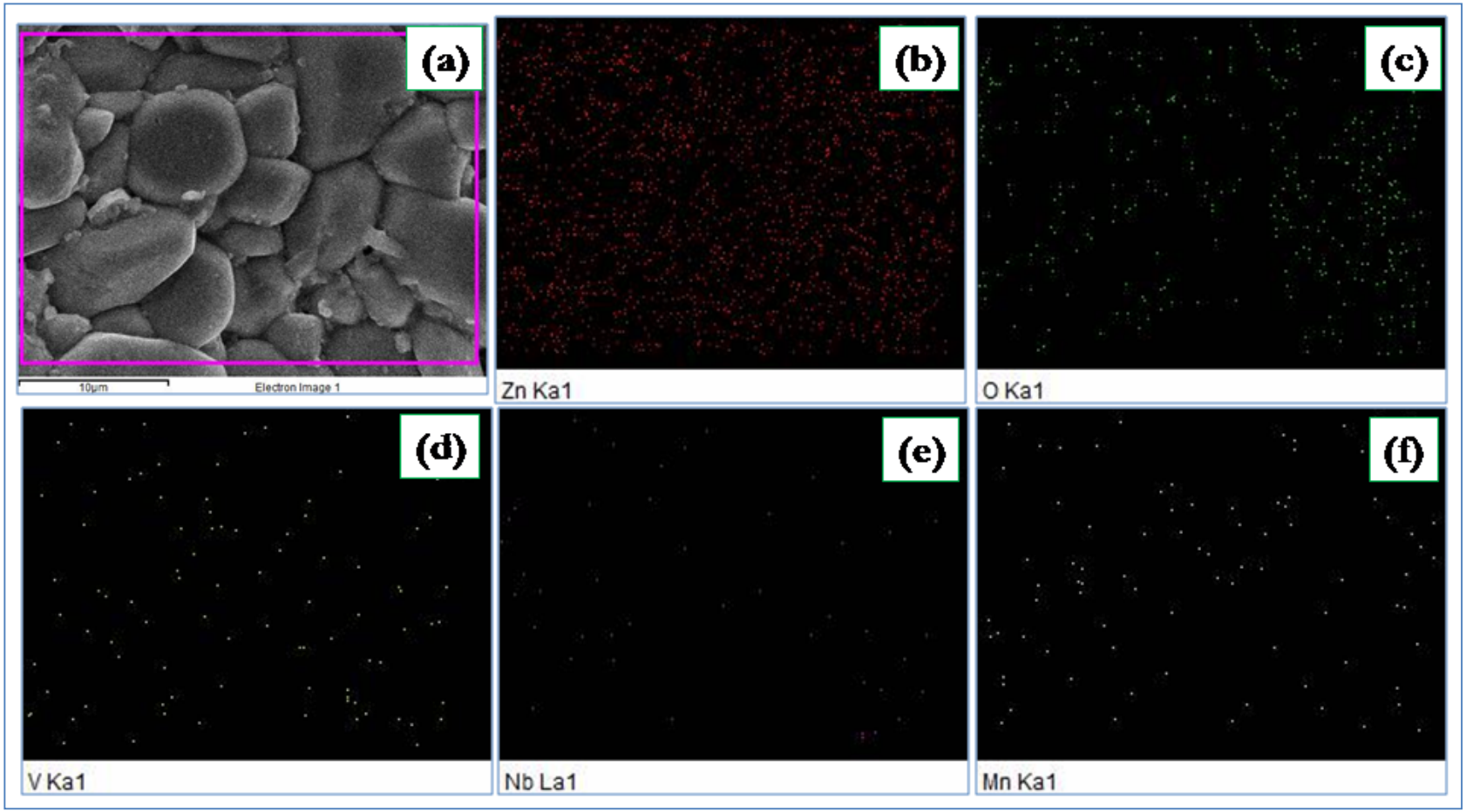

Figure 6.10: EDS elemental maps for 2.50 mol% MnO Doped ZnO-V_2O_5-Nb_2O_5 System (900NM250) sintered at 900 °C: (a) SEM micrograph (b) Zn map (c) O map (d) V map (e) Nb map and (f) Mn map.

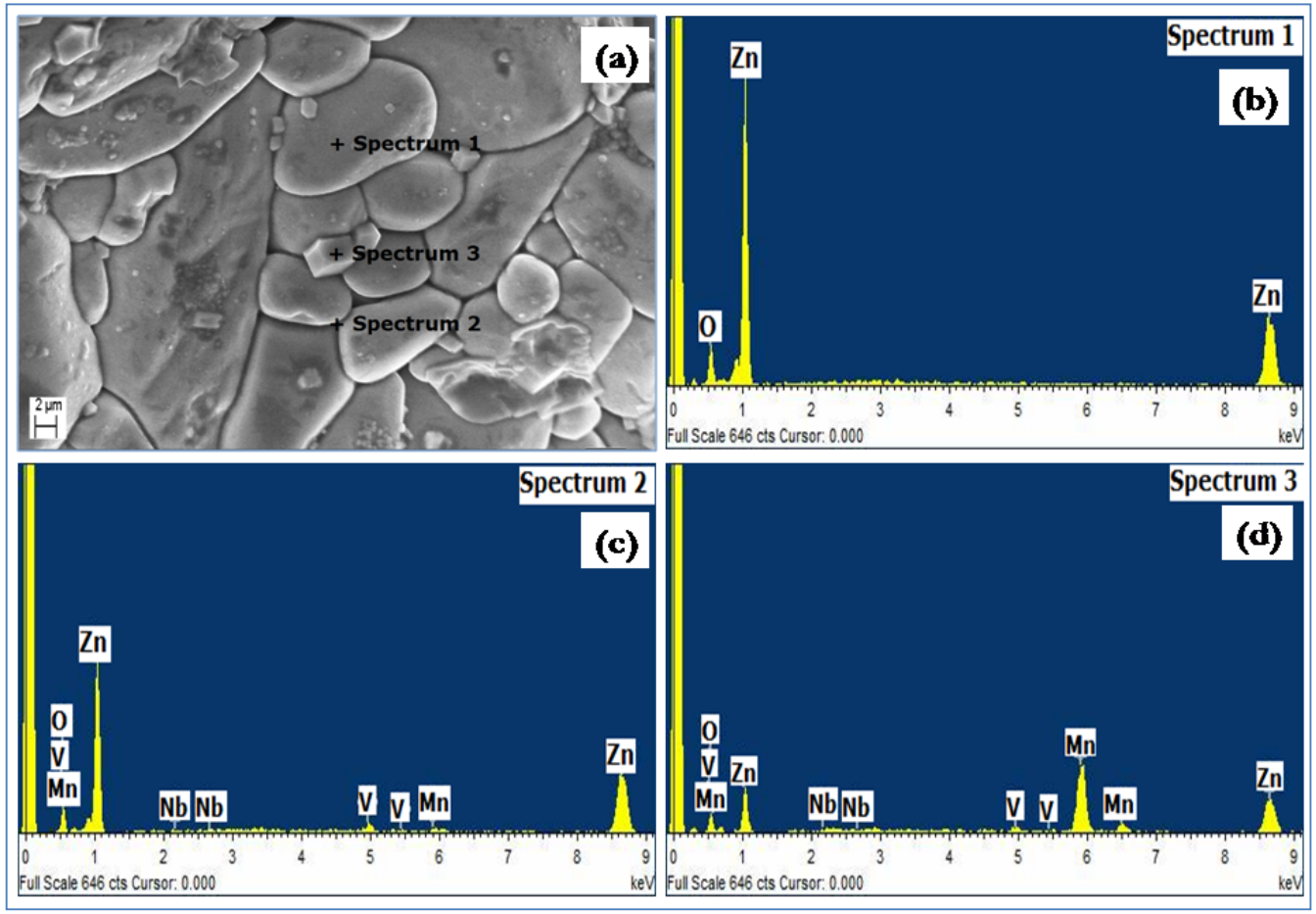

Figure 6.11: EDS spectra of 2.50mol% MnO Doped ZnO-V_2O_5-Nb_2O_5 System (950NM250) sintered at 950 °C: (a) SEM micrograph (b) at the ZnO grain (c) at the ZnO grain boundary showing V, Nb and Mn segregation in it and (d) at the selected region.

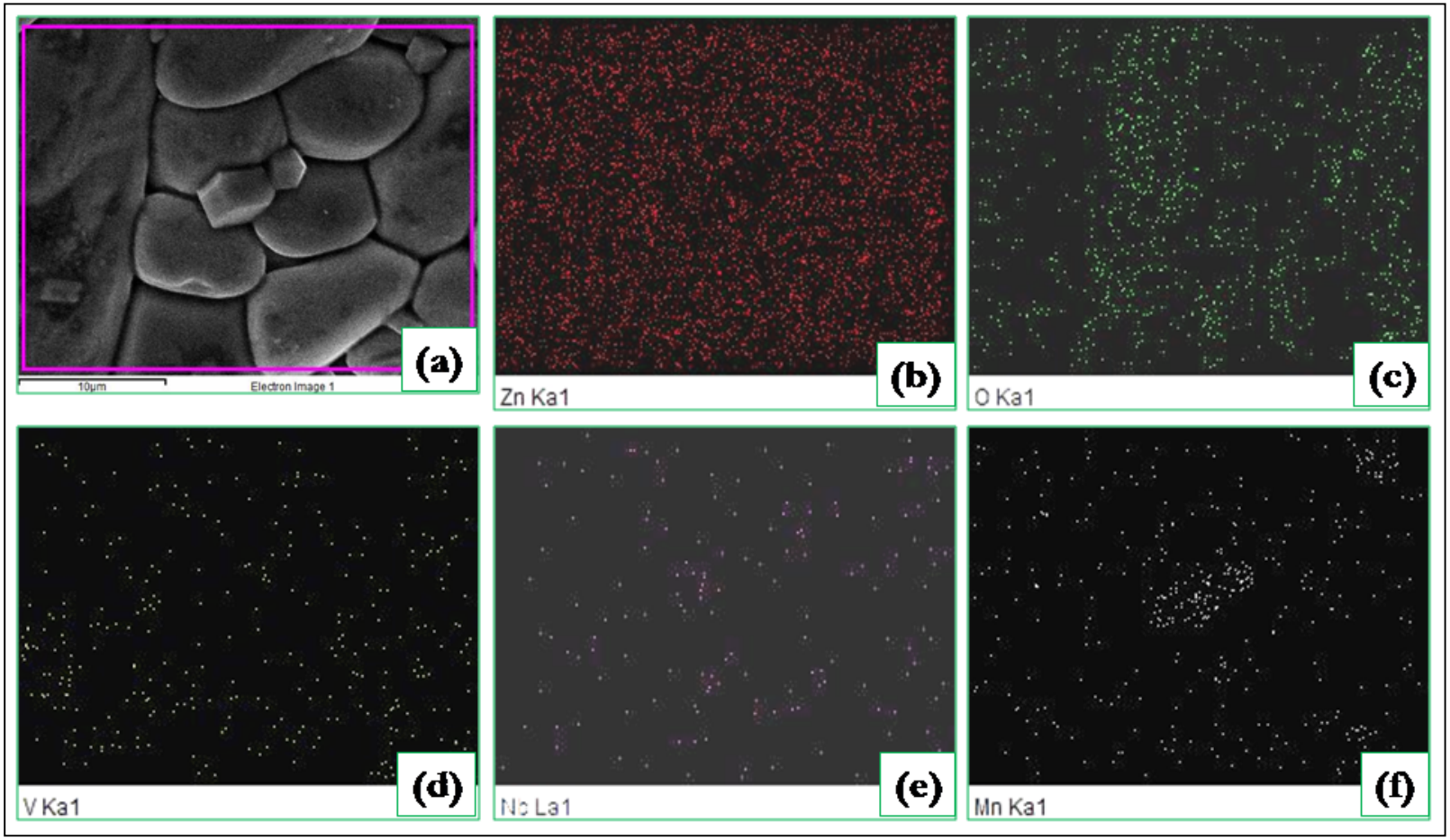

Figure 6.12: EDS elemental maps for 2.50 mol% MnO Doped ZnO-V_2O_5-Nb_2O_5 System (950NM250) sintered at 950 °C: (a) SEM micrograph (b) Zn map (c) O map (d) V map (e) Nb map and (f) Mn map.

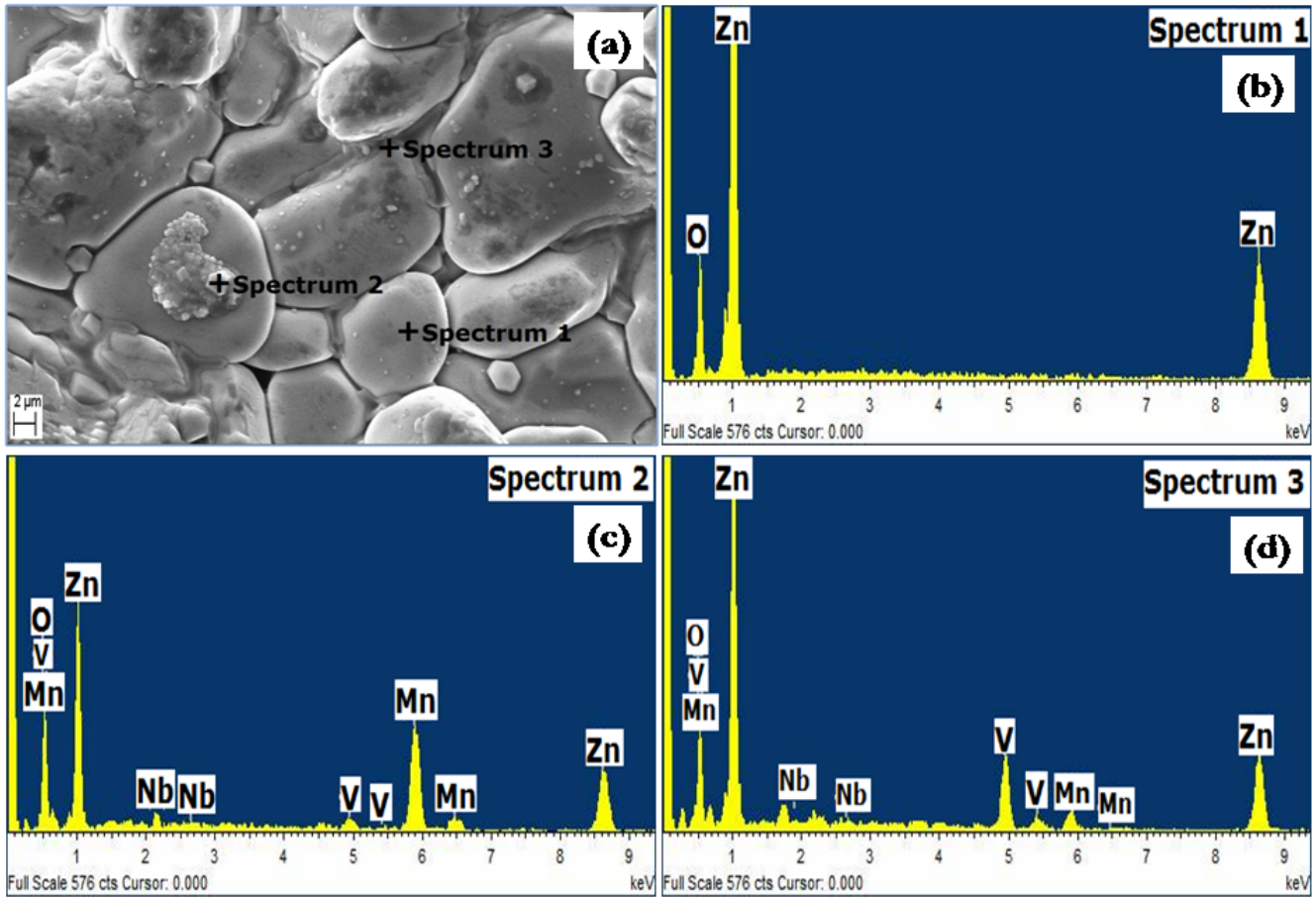

Figure 6.13: EDS spectra of 3.00 mol MnO Doped ZnO-V_2O_5-Nb_2O_5 System (950NM300) sintered at 950 °C: (a) SEM micrograph (b) at the ZnO grain (c) at the ZnO grain boundary showing V, Nb and Mn segregation in it and (d) at the selected region.

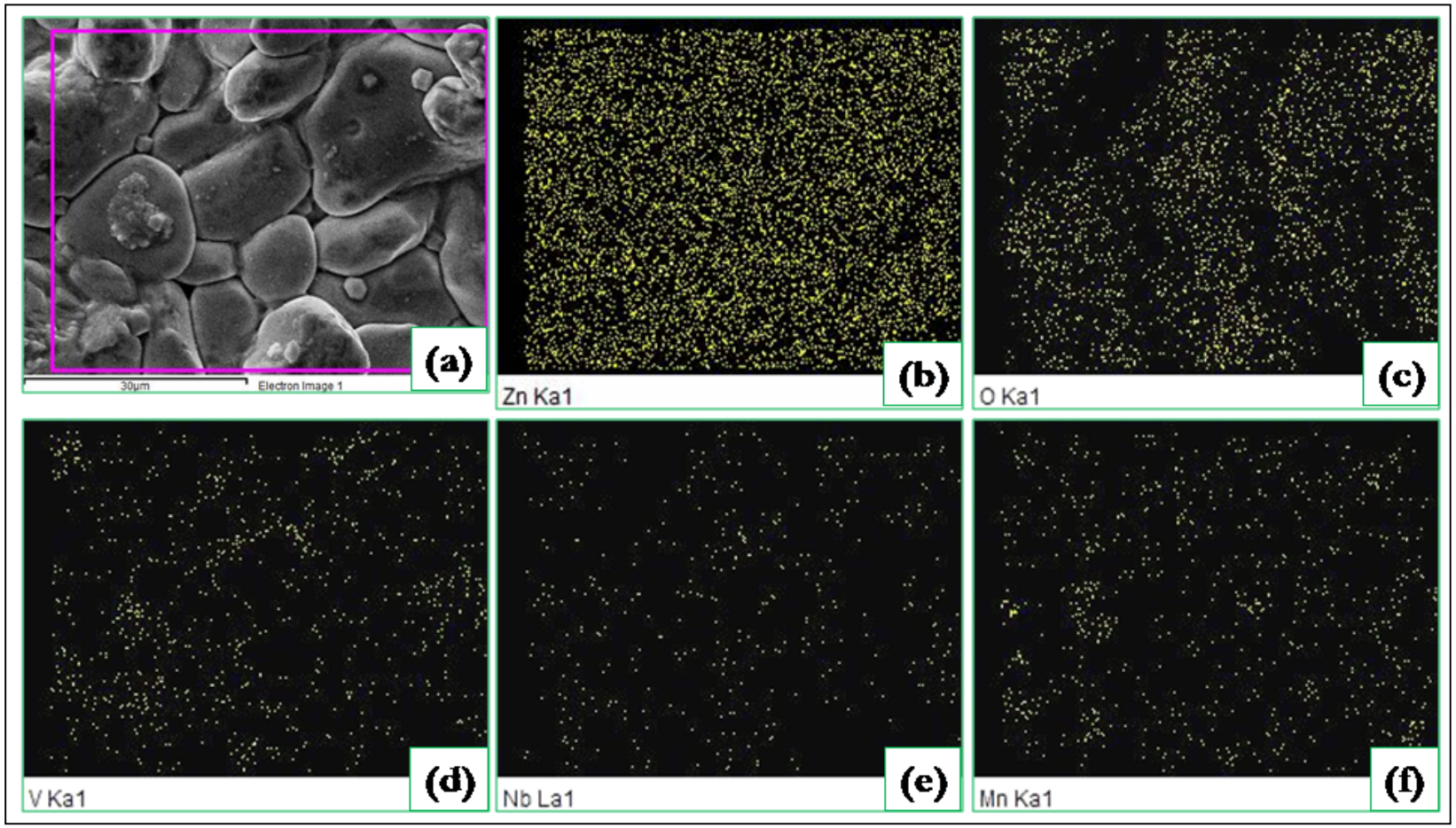

Figure 6.14: EDS elemental maps for 3.00 mol% MnO Doped ZnO-V_2O_5-Nb_2O_5 System (950NM300) sintered at 950 °C: (a) SEM micrograph (b) Zn map (c) O map (d) V map (e) Mn map and (f) Nb map.

6.1.4. Percentage Theoretical Density

Fig. 6.15(a) shows the plot between percentage theoretical density vs. mol% MnO for the samples sintered at 850˚C. The sintered density of the samples sintered at 850 ˚C was found to be in the range approximately 5.32-5.39 gm/cc given in Table 6.1, corresponding to 93.55-94.88 % of the theoretical density (TD). Table 6.4 shows the percentage theoretical density for 0.00, 1.50, 2.00, 2.50 and 3.00 mol% MnO-doped samples are 93.55, 94.47, 94.55, 94.83 and 94.88 % respectively. The value of percentage theoretical density increases with MnO doping

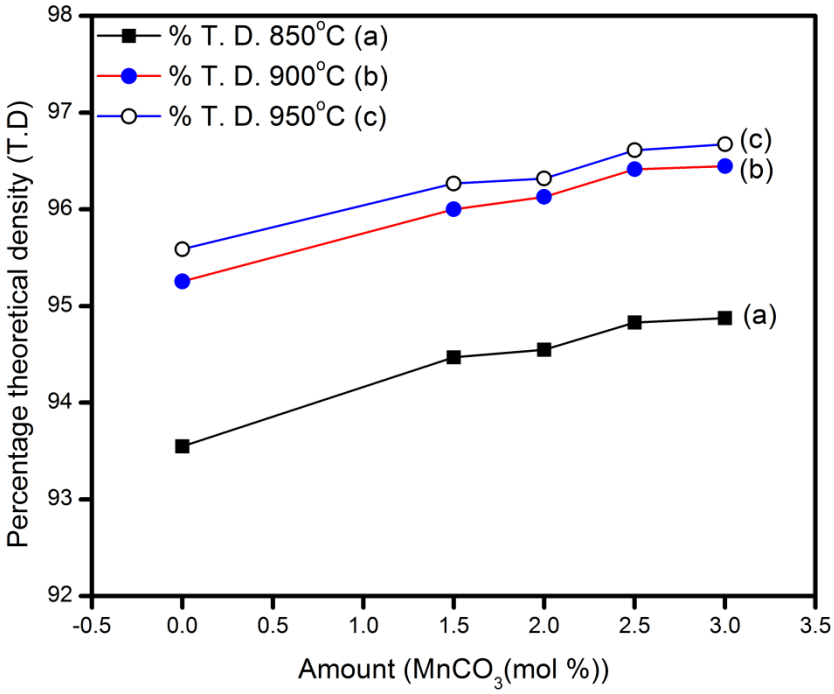

Fig. 6.15: shows the plot of percentage theoretical density vs. mol% MnO for the samples sintered at (a) 850 °C, (b) 900 °C & (c) 950 °C

Fig. 6.15(b) shows the plot between percentage theoretical density vs. mol% MnO for the samples sintered at 900 ˚C. The sintered density of the samples sintered at 900 ˚C were found to be approximately 5.427-5.481 gm/cc given in Table 6.2, corresponding to 95.25-96.45% of the theoretical density (TD). Table 6.5 shows the percentage theoretical density for 0.00, 1.50, 2.00, 2.50 and 3.00 mol% MnO-doped samples are 95.25, 95.99, 96.13, 96.41 and 96.45 % respectively.

Fig. 6.15(c) shows the plot between percentage theoretical density vs. mol% MnO for the samples sintered at 950 ˚C. The sintered density of the samples sintered at 950 ˚C was found to be in the range approximately 5.43-5.49 gm/cc given in Table 6.3, corresponding to 95.59-96.67% of the theoretical density (TD). Table 6.6 shows the percentage theoretical density for for 0.00, 1.50, 2.00, 2.50 and 3.00 mol% MnO-doped samples are 95.59, 96.27, 96.32, 96.61 and 96.67 respectively. Sample 950NM250 shows the high value of density (5.49 gm/cc). It was assumed that the decrease of the sintered density is ascribed to the volatility of the V-species for V_2O_5 with a low melting point.

6.2. Electrical Behavior of MnO Doped $ZnO\text{-}V_2O_5\text{-}Nb_2O_5$ Varistor.

6.2.1. Non-Linear Properties

The varistor properties are featured by the conduction characteristics, which do not follow Ohm's law in the E–J relation. Basically, the curves are divided into two regions: one is a linear insulating region with high resistance before breakdown field and other is a nonlinear conducting region with low resistance after the breakdown field. The sharp knee of the curves leads to the better varistor properties.The behaviour of E_{1mA} in accordance with MnO content can be explained by the following expression:

$$E_{1mA} = V_{gb}/d, \tag{6.1}$$

where d is the grain size, and V_{gb} is the breakdown voltage per grain boundary. This expression indicates that the V_{gb} value is directly determined from E_{1mA} [Levinson (1975)].

Fig. 6.16 shows the electric field–current density (E–J) characteristics of the samples sintered at 850 °C. The breakdown field (E_{1mA}) increased from 353.4 to 732.8 V/mm and then decreased to 426.1 V/mm with the further increase of the Mn content. Therefore, the decrease of E_{1mA} with the increase of the Mn content is attributed to the decrease of the breakdown voltage per grain boundary and the increase of the average ZnO grain size.The leakage current density decreased from 372.5 to 184.1 μA/cm^2 with increasing content of Mn. However, further increase in the Mn content caused J_L to increase to 226.9 μA/cm^2, as shown in Fig. 6.16. The increase of J_L is attributed to the increase of the minority carriers in the grain boundary.

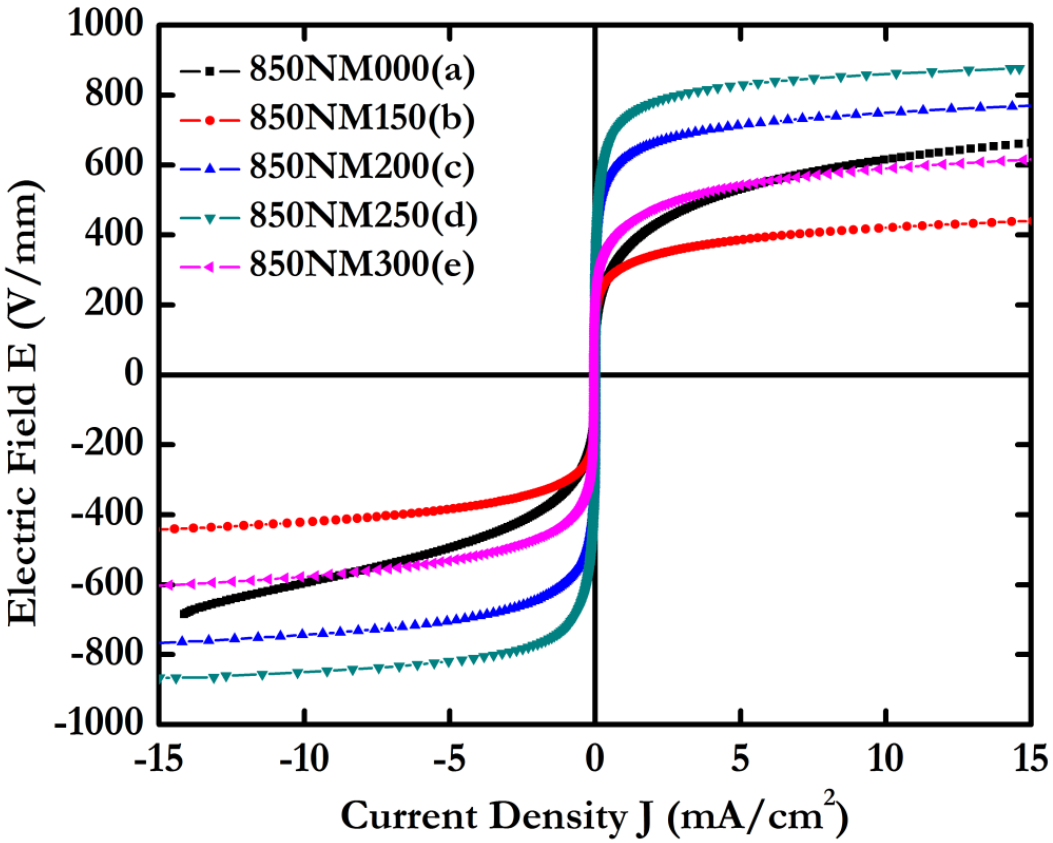

Figure 6.16: E-J curve showing the effects of MnO content in ZnO-V_2O_5-Nb_2O_5 samples sintered at 850°C: (a) 850NM000 (0.00 mol% MnO); (b) 850NM150 (1.50 mol% MnO); (c) 850NM200 (2.00 mol% MnO); (d) 850NM250 (2.50 mol% MnO) and (e) 850NM300 (3.00 mol% MnO)

Table 6.7: Summary of electrical results obtained for MnO doped ZnO-V_2O_5-Nb_2O_5 varistors sintered at 850 °C

Sample Name	Non-ohmic coefficient α	Breakdown field (V/mm)	Leakage current density J_L (μA/cm²)	Vgb (V/gb)	ε' (1KHz)	Tan δ (1KHz)
850NM000	4.5	353.4	372.5	1.85	316	0.285
850NM150	7.5	310.8	168.1	1.79	414	0.153
850NM200	12.1	619.4	112.1	3.43	309	0.151
850NM250	14.2	732.8	184.1	3.96	263	0.127
850NM300	7.0	426.1	226.9	2.20	354	0.174

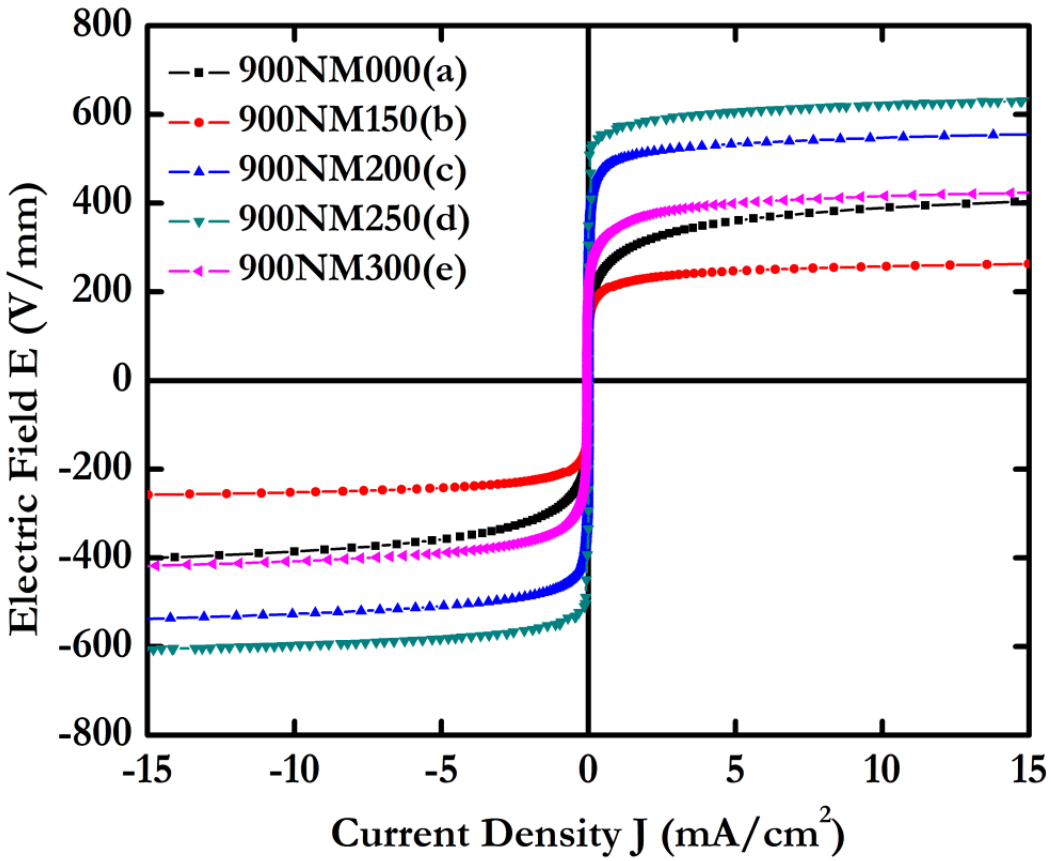

Figure 6.17: E-J curve showing the effects of MnO content in ZnO-V_2O_5-Nb_2O_5 samples sintered at 900°C: (a) 900NM000 (0.00 mol% MnO); (b) 900NM150 (1.50 mol% MnO); (c) 900NM200 (2.00 mol% MnO); (d) 900NM250 (2.50 mol% MnO) and (e) 900NM300 (3.00 mol% MnO)

Table 6.8: Summary of electrical results obtained for MnO doped ZnO-V_2O_5-Nb_2O_5 varistors sintered at 900 °C

Sample name	Non-ohmic coefficient α	Breakdown field E (V/mm)	Leakage current density J_L(μA/cm²)	Vgb (V/gb)	ε' (1KHz)	Tan δ (1KHz)
900NM000	7.1	281.5	310.577	1.99	718	0.079
900NM150	13.2	217.1	110.939	3.38	770	0.161
900NM200	24.3	498.5	63.114	4.59	384	0.117
900NM250	28.3	572.6	51.204	4.81	312	0.152
900NM300	13.5	349.9	145.208	3.26	543	0.193

The nonlinear coefficient (α) was increased from 4.5 to 14.2 with increasing content of Mn. However, further increase caused α to decrease upto 7.0, as shown in Fig. 6.16. As a result, it can be seen that the Mn content has a significant effect on the nonlinear properties of these ceramics in light of a variation. The E–J characteristic parameters are summarized in Table 6.7. The reduction in the number of grain boundaries per unit thickness due to grain enlargement should have caused of decrease in α value.

Fig. 6.17 shows the electric field–current density (E–J) characteristics of the samples sintered at 900 °C. The breakdown field (E_{1mA}) increased from 281.5 to 572.6 V/mm and then decreased to 349.9 V/mm with the increase of the Mn content. Therefore, the decrease of E_{1mA} with the increase of the Mn content is attributed to the decrease of the breakdown voltage per grain boundary and the increase of the average ZnO grain size. The leakage current density decreased from 310.5 to 51.2 μA/cm^2 with increasing content of Mn. However, further increase in the Mn content caused J_L to increase to 145.208 μA/cm^2, as shown in Fig. 6.17. The increase of J_L is attributed to the increase of the minority carriers in the grain boundary.

Fig. 6.18 shows the electric field–current density (E–J) characteristics of the samples sintered at 950°C. The breakdown field (E_{1mA}) increased from 128.7 to 191.4 V/mm and then decreased to 136.9 V/mm with the increase of the Mn content. Therefore, the decrease of E_{1mA} with the increase of the Mn content is attributed to the decrease of the breakdown voltage per grain boundary and the increase of the average ZnO grain size. The leakage current density decreased from 385.801 to 36.461 μA/cm^2 with increasing content of Mn. However, further increasing Mn content caused J_L to increase to 359.345 μA/cm^2, as shown in Fig. 6.18. The increase of J_L is attributed to the increase of the minority carriers in the

grain boundary.

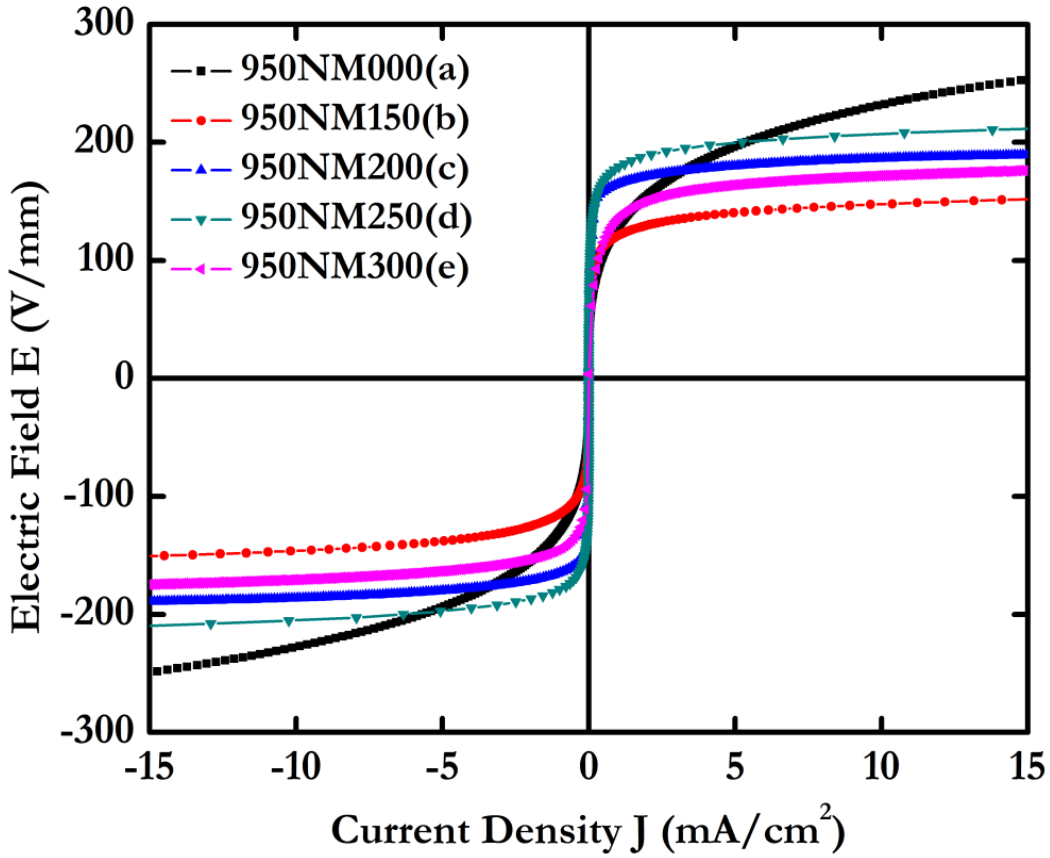

Figure 6.18: E-J curve showing the effects of MnO content in ZnO-V_2O_5-Nb_2O_5 samples sintered at 950°C: (a) 950NM000 (0.00 mol% MnO); (b) 950NM150 (1.50 mol% MnO); (c) 950NM200 (2.00 mol% MnO); (d) 950NM250 (2.50 mol% MnO) and (e) 950NM300 (3.00 mol% MnO)

Table 6.9: Summary of Electrical Results obtained for MnO doped ZnO-V_2O_5-Nb_2O_5 materials sintered at 950 °C

Sample name	Non-ohmic coefficient α	Breakdown field E_{1mA} (V/mm)	Leakage current density J_L (μA/cm²)	Vgb (V/gb)	ε' (1KHz)	Tan δ (1KHz)
950NM000	4.2	128.7	385.801	1.301	927	0.189
950NM150	11.6	121.4	125.243	1.962	1970	0.145
950NM200	18.9	165.5	129.652	2.778	1046	0.184
950NM250	21.6	191.4	36.461	3.038	793	0.101
950NM300	9.9	136.9	359.345	2.538	1302	0.156

The nonlinear coefficient (α) was increased from 4.2 to 21.6 with increasing content of Mn. However, further increase caused α to decrease upto 9.9, as shown in Fig. 6.18. As a result, it can be seen that the Mn content has a significant effect on the nonlinear properties of these ceramics in light of a variation. The E–J characteristic parameters are summarized in Table 6.9.

The reduction in the number of grain boundaries per unit thickness due to grain enlargement should have caused a decrease in α value. This suggests that segregation of Mn in the grain boundary promoted the development of the essential potential barrier at the interface. Adversely, excessive Mn doping encouraged thicker grain bondary formation that could lead to poor non-linearity and lower bulk resistance. The behaviour of α in accordance with the Mn content can be related to the variation of the Schottky barrier height according to the variation of the electronic states at the grain boundaries.

The non-linear property of the varistors is explained by the existence of potential barrier at the grain boundaries. In practice, there are a variety of inter-grain conduction paths that operate in parallel in varistors. They operate through the grain boundary region or through the bulk inter-granular material. In fact, transition metal oxides are involved in the formation of interfacial states and deep bulk traps at grain boundaries, providing large potential barriers to give better nonlinear characteristics. This barrier is schottky type in which, conduction in linear region is dominated by thermionic emission over this schottky barrier. Thus it is clear that vanadium ions play an important role in the non-linear conductivity of the prepared ceramics and it is important to discuss the defect chemistry induced by doping ZnO with V_2O_5.

6.2.2. Dielectric Spectroscopy

Fig. 6.19 shows the dielectric characteristics of the samples sintered at 850 °C with different amounts of MnO.The ε' and tan δ at 1KHz for the 0.00, 1.50, 2.00, 2.50 and 3.00 mol% MnO-doped ZnO–V_2O_5–Nb_2O_5 samples sintered at 850ºC are 316, 414, 309, 263, 354 and 0.285, 0.153, 0.151, 0.127, 0.174 respectively given in Table 6.7. At lower frequencies, a high relative dielectric permittivity was found. The dispersion of the dielectric properties is obvious. The formation of the grain boundary barrier layer was also confirmed by the rapid decrease of the apparent dielectric constant with increasing frequency of the ceramics and the non-ohmic I-V behaviour.

Fig. 6.20 shows the dielectric characteristics of the samples sintered at 900°C with different amounts of MnO. The ε' and tan δ at 1KHz for the 0.00, 1.50, 2.00, 2.50 and 3.00 mol% MnO-doped ZnO–V_2O_5–Nb_2O_5 samples sintered at 900°C are 719, 770, 384, 312, 543 and 0.079, 0.161, 0.117, 0.152, 0.193 respectively given in Table 6.8. Heterogeneities in the grains and/or the presence of the potential barriers between the grains are responsible for the similar dielectric properties in a number of materials. Orientational polarization (zinc interstitials and oxygen vacancies) is dominant at higher frequencies, whereas the high degree of dispersion observed at the low-frequency region is attributable to interfacial polarization [Hanada (2009)].

Fig. 6.21 shows the dielectric characteristics of the samples sintered at 950°C with different amounts of MnO. The ε' and tan δ at 1KHz for the 0.00, 1.50, 2.00, 2.50 and 3.00 mol% MnO-doped ZnO–V_2O_5–Nb_2O_5 samples sintered at 950°C are 927, 1970, 1046, 793, 1302 and 0.189, 0.145, 0.184, 0.101, 0.156 respectively given in Table 6.9. As the amount of MnO increased, the dielectric constant (έ) decreased with less sharp dispersive drop with increasing frequency, which is closely associated with the polarization of dielectrics. It is assumed that this is attributed to the decrease of the number of dipole, which can follow the test frequency.

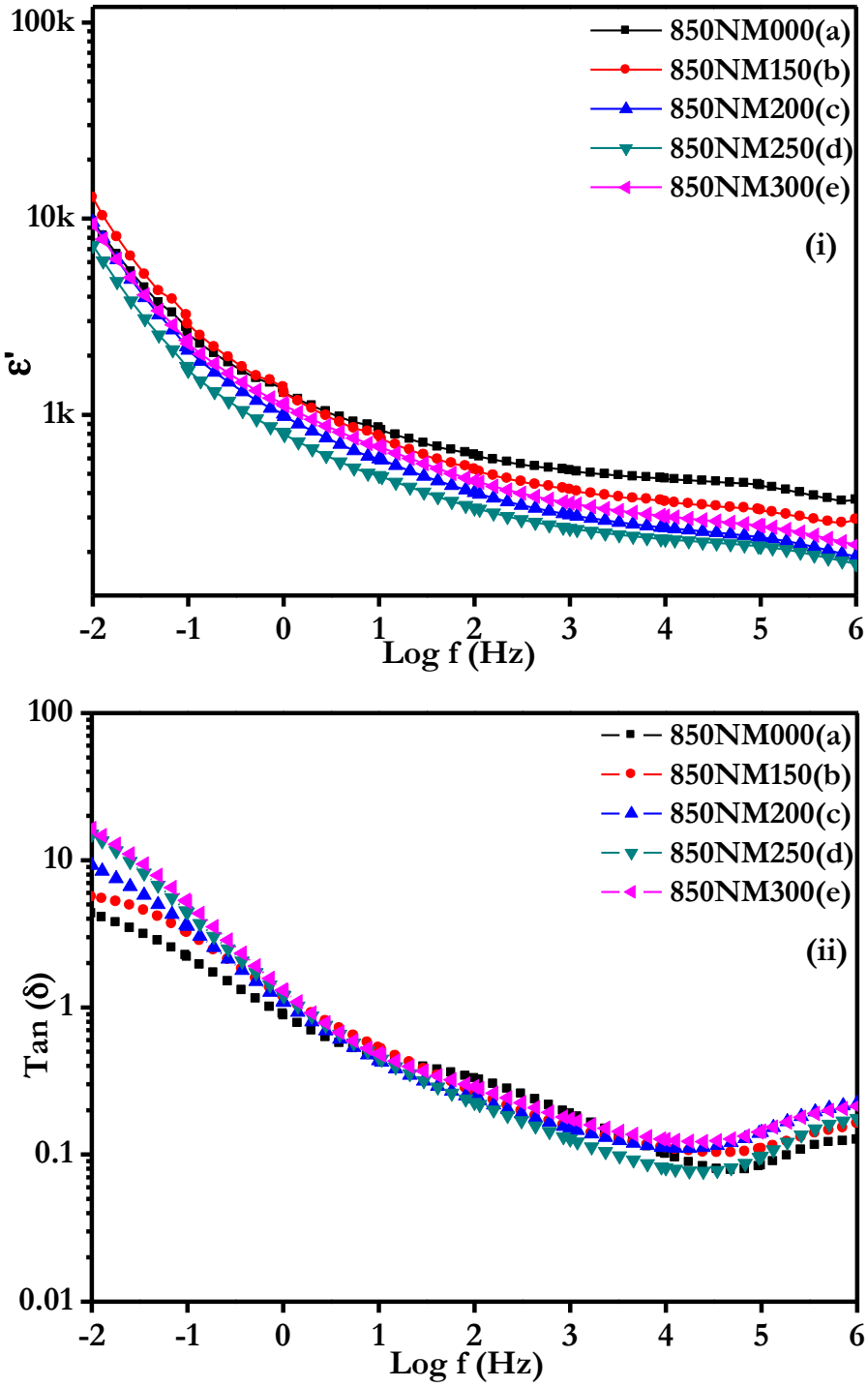

Figure 6.19: Dielectric spectroscopy (i) ε'and (ii) Tan δ, showing the effects of MnO content in ZnO-V_2O_5-Nb_2O_5 materials: (a) 850NM000 (0.00 mol% MnO); (b) 850NM150 (1.50 mol% MnO); (c) 850NM200 (2.00 mol% MnO); (d) 850NM250 (2.50 mol% MnO) and (e) 850NM300 (3.00 mol% MnO).

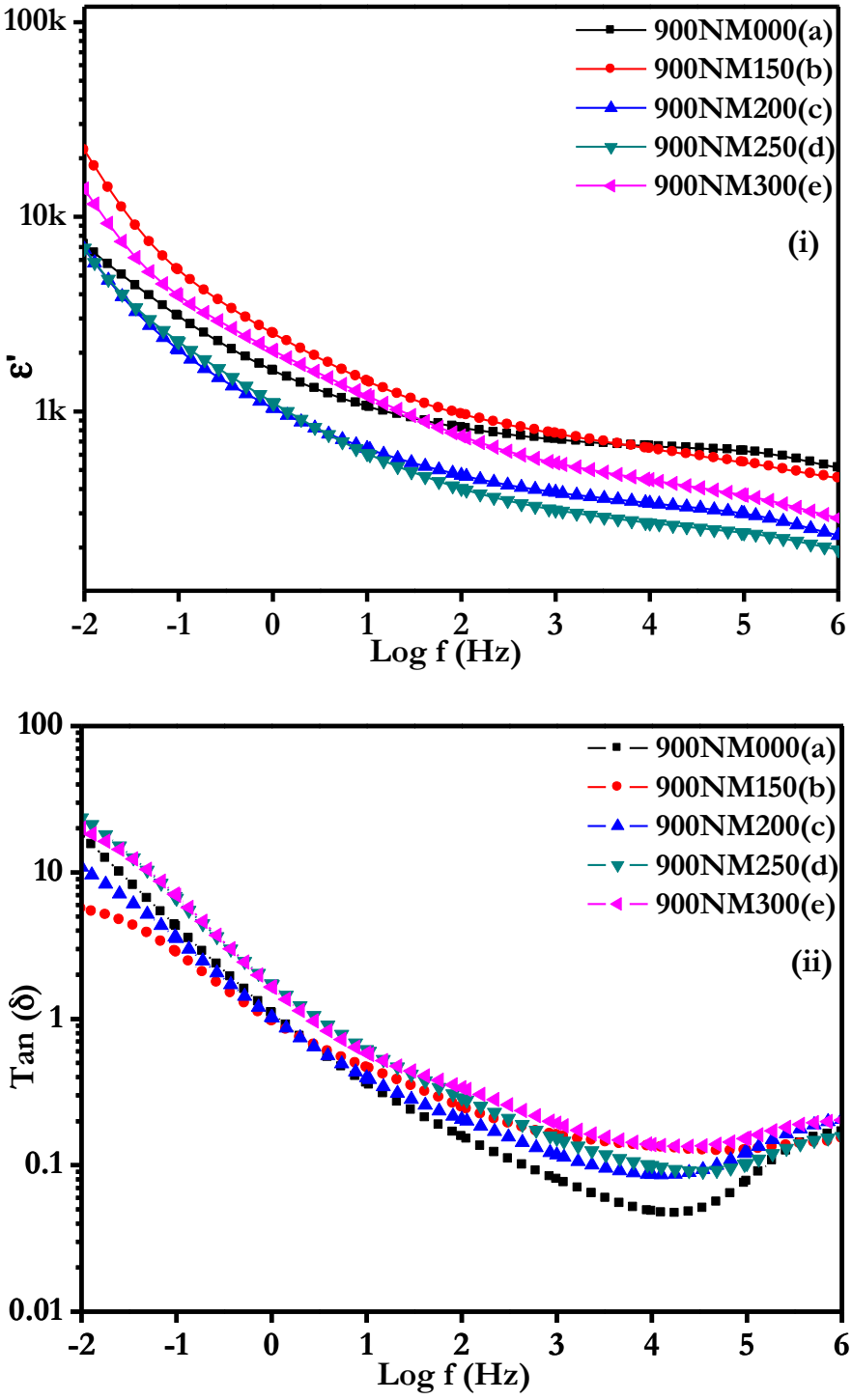

Figure 6.20: Dielectric spectroscopy (i) ε' and (ii) Tan δ, showing the effects of MnO content in ZnO-V_2O_5-Nb_2O_5 materials: (a) 900NM000 (0.00 mol% MnO); (b) 900NM150 (1.50 mol% MnO); (c) 900NM200 (2.00 mol% MnO); (d) 900NM250 (2.50 mol% MnO) and (e) 900NM300 (3.00 mol% MnO)

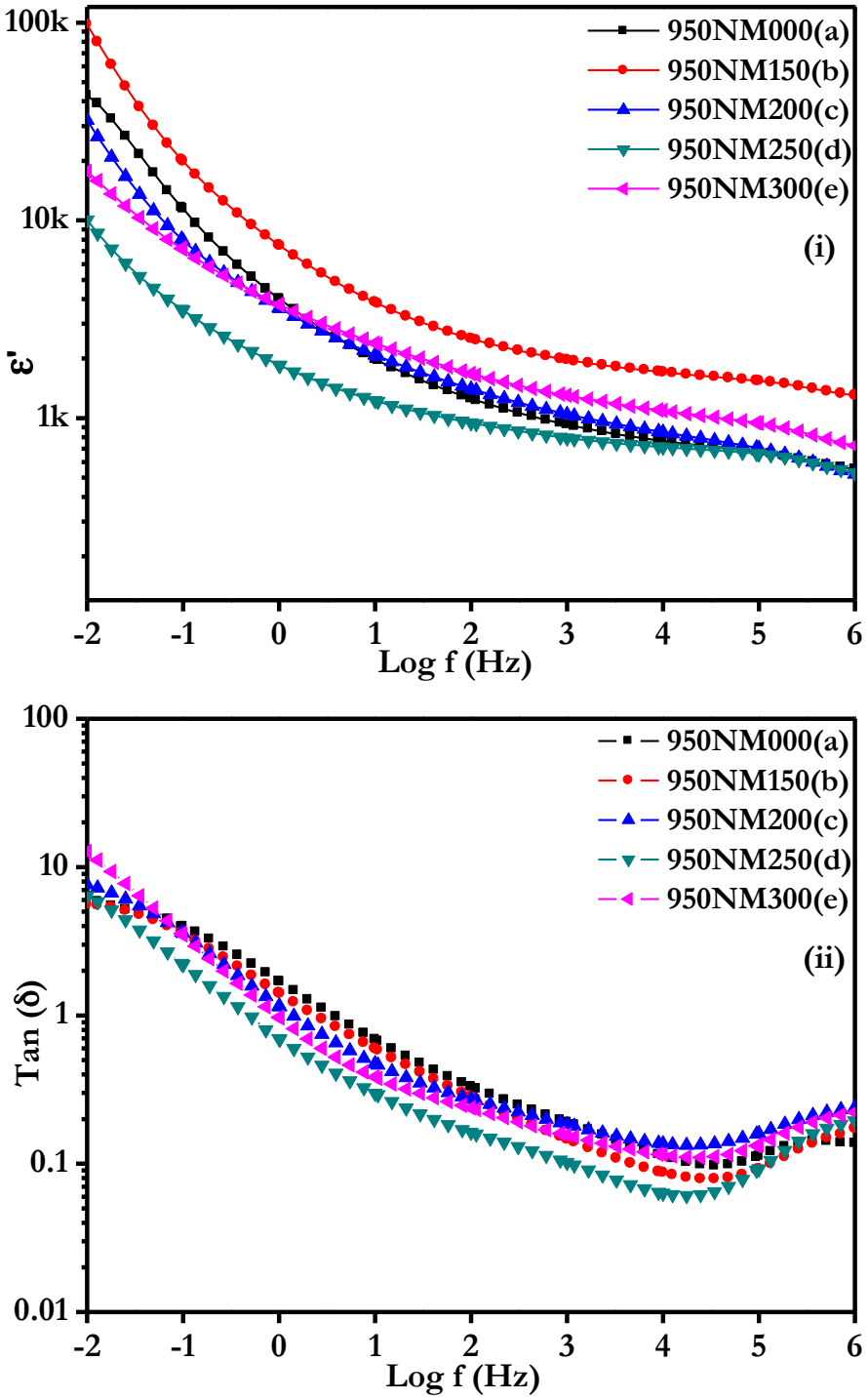

Figure 6.21: Dielectric spectroscopy (i) ε' and (ii) Tan δ, showing the effects of MnO content in ZnO-V_2O_5-Nb_2O_5 materials: (a) 950NM000 (0.00 mol% MnO); (b) 950NM150 (1.50 mol% MnO); (c) 950NM200 (2.00 mol% MnO); (d) 950NM250 (2.50 mol% MnO) and (e) 950NM300 (3.00 mol% MnO)

It is observed that the ε' measuring within the frequency depends on the amount of MnO. This is directly related to the average grain size and depletion layer width, as can be seen in the following expression:

$$\varepsilon' = \mathcal{E}_g \frac{d}{t} \tag{6.2}$$

where έ is the dielectric constant of ZnO (8.5), d is the average grain size, and t is the depletion layer width of the both sides at the grain boundaries. The decrease of d/t ratio in $\varepsilon' = \mathcal{E}_g \frac{d}{t}$ gives rise to the decrease of the ε'. For the samples sintered at 900°C, the έ at 1 kHz decreased from 718.6 to 43.4. The detailed dielectric parameters are summarized in Tables from 6.7 to 6.9.

6.2.3. Impedance Spectroscopy

The semicircle curves observed in Figs. 6.22 to 6.30 (a-e). It was analysed by convolution of two time constant in the system. Thus, the equivalent circuit containing two parallel resistance-constant phase element (CPE) sub-circuits in series was used for fitting the impedance spectra which is shown from Figs. 6.22 to 6.30 (f). Use of a simple capacitor is not adequate to model the electrical response of the material due to the microstructural heterogeneities of the sample. The appearance of full and partial semicircles or no semicircle depends upon the strength of relaxation and the available frequency range [Bueno et al. (1998); Pattanayak et al. (2014); Choudhary et al. (2013); West et al. (1997)], although these semicircles are depressed. This behaviour manifests that there is a distribution of relaxation times instead of a single relaxation time in the material and confirms the presence of a non-debye type relaxation in the materials. In most real cases related to ceramic materials, the Nyquist plot is depressed, with its centre below the real axis. A perfect semicircle with its centre on the Z'-axis is observed for ideal debye-type relaxation. However, in the studied material, we did not find such debye-type relaxation [Tsai et al. (1994); (1996)]. A constant phase element (CPE) is used to represent the non-ideal debye type behaviour, which has impedance given by Abram et al. [2003], and is introduced with the resistors and capacitors or a CPE.The CPE is equivalent to a

distribution of capacitors in parallel. The impedance function of the CPE element is

$$Z_{CPE} = \frac{1}{P(j\omega)^n} \quad (6.3)$$

where P is a constant that is independent of frequency, ω = 2πf is the angular frequency (f is the applied frequency in Hz), $j = \sqrt{-1}$ and n is an exponential index, which is measure of arc depression. When constant n = 0, the CPE acts as a pure resistor with value = $1/P$, while n = 1 for ideal debye-like behaviour, in which, the CPE represents an ideal capacitor (C = P). The capacitor is frequency dependent when the n value is below unity. In most real cases of ceramic materials, the arc in complex impedance plots of Im (Z') versus Re (Z") is depressed, with its centre below the real axis. However, in polycrystalline semiconductor ceramics, the trapping of the charge at grain boundaries appears to have a significant effect on the electrical transport properties due to the formation of electrostatic potential barriers [Abram (2003)].

The electrode contribution to the overall electrolyte resistance has not been considered. A total of three regions were apparent. One region appears to be the highly conducting grain cores and was not considered further [West et al. (1997)].The other two regions represent the grain boundary regions that further split into low- and high-frequency regions; these regions were considered further in this work. Two hypotheses may be considered to explain these two time constants. The first hypothesis suggests that one time constant is related to the grain barrier and the second is associated with the grain boundary barrier. The limitation of this model is that the grain resistivity calculated at 50°C, 150°C & 250°C is higher than the literature values reported for grain resistivity of ZnO [West et al. (1997)]. The second hypothesis of the existence of different defects and/or adsorbed species at the grain boundary region, not necessarily at the same grain boundary. The two time constants may be the result of these types of defects. The second hypothesis is more feasible because the possibility of existence of different adsorbed species and defects on ZnO was observed in the literature [Bueno et al. (1998)].

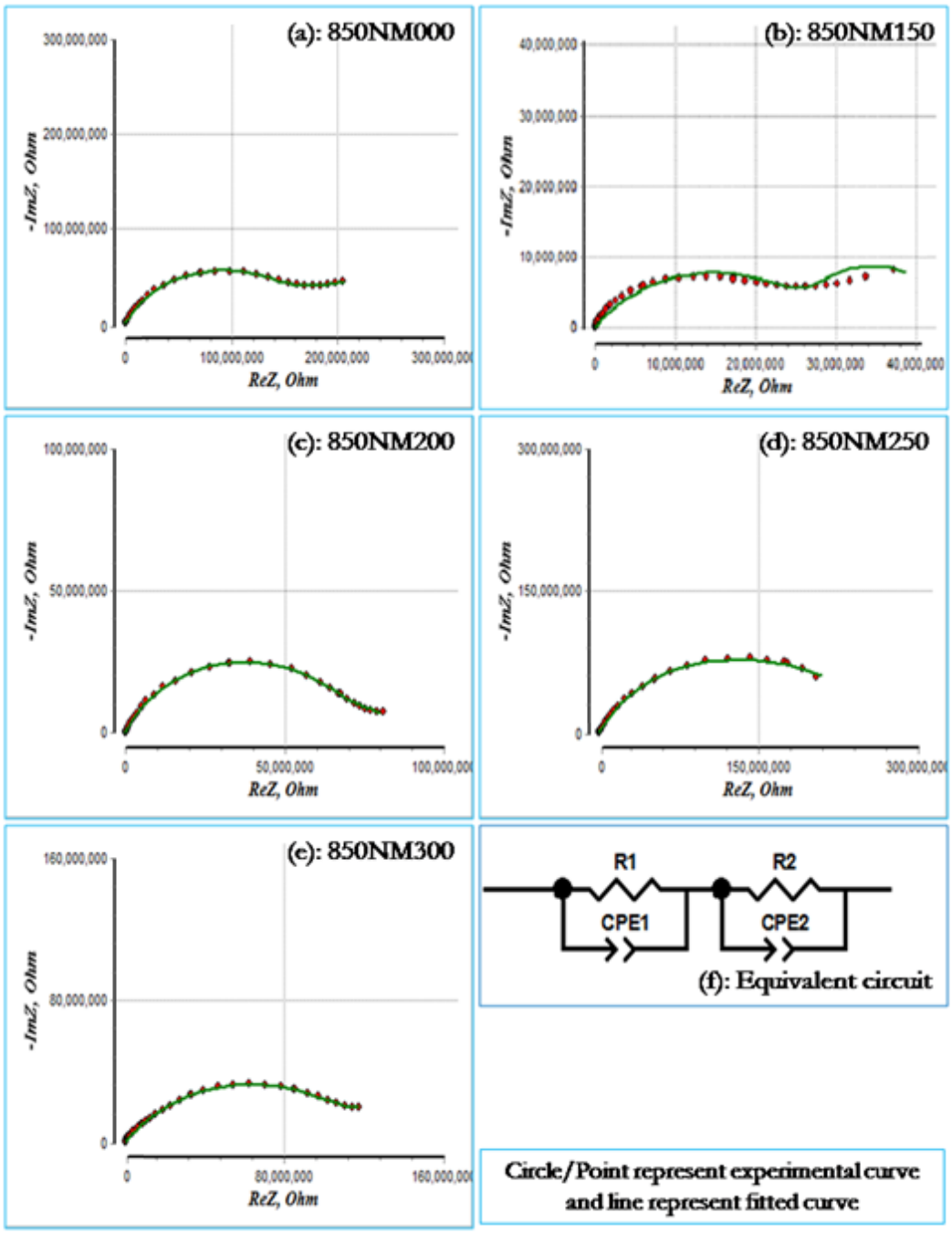

Figure 6.22: Experimental plots, fitted plots and equivalent circuit for fitting of impedance spectra of the samples as a function of MnO amount measured at 50°C : (a) 850NM000 (0.00 mol% MnO); (b) 850NM150 (1.50 mol% MnO); (c) 850NM200 (2.00 mol% MnO); (d) 850NM250 (2.50 mol% MnO); (e) 850NM300 (3.00 mol% MnO) and (f) equivalent circuit.

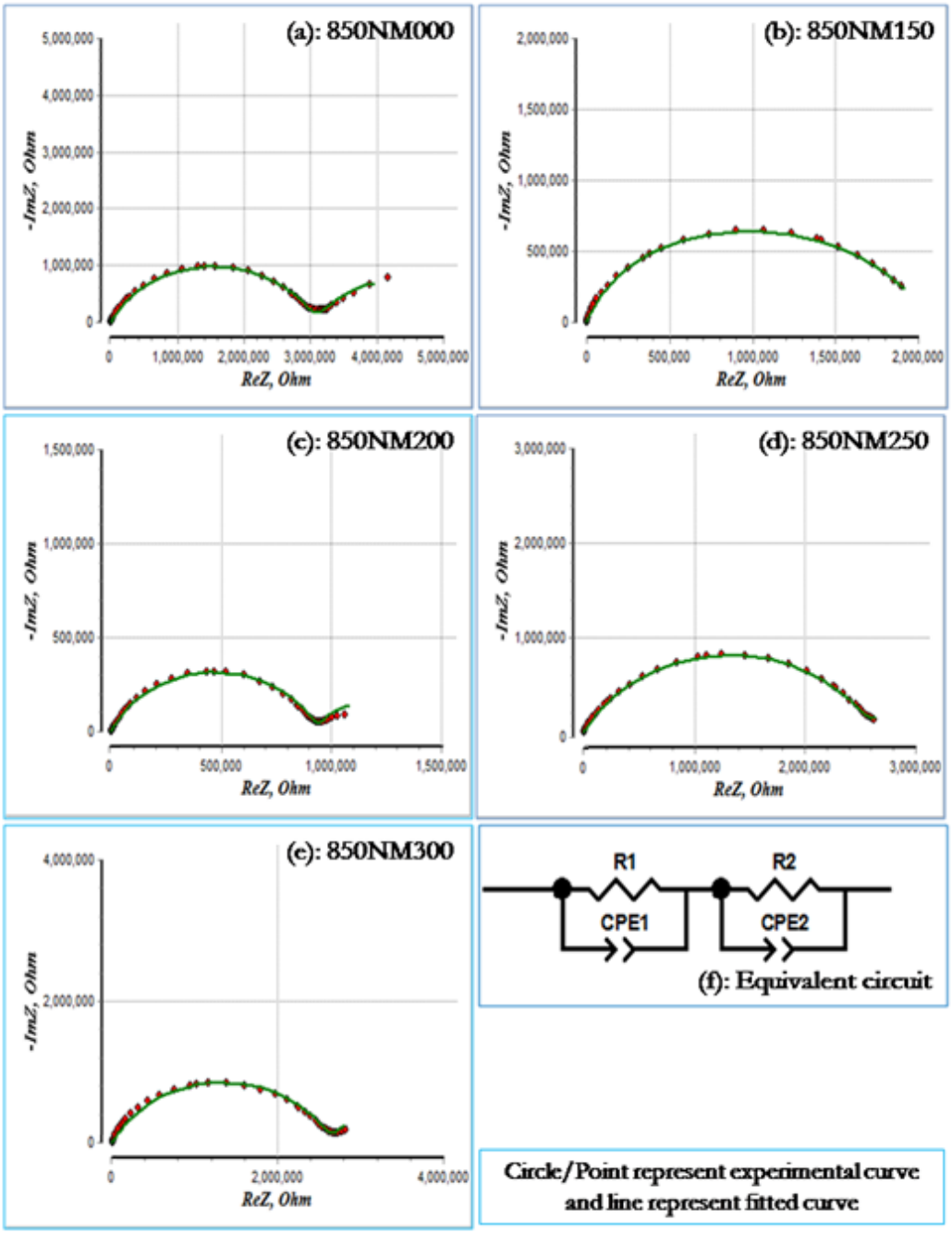

Figure 6.23: Experimental plots, fitted plots and equivalent circuit for fitting of impedance spectra of the samples as a function of MnO amount measured at 150°C : (a) 850NM000 (0.00 mol% MnO); (b) 850NM150 (1.50 mol% MnO); (c) 850NM200 (2.00 mol% MnO); (d) 850NM250 (2.50 mol% MnO); (e) 850NM300 (3.00 mol% MnO) and (f) equivalent circuit.

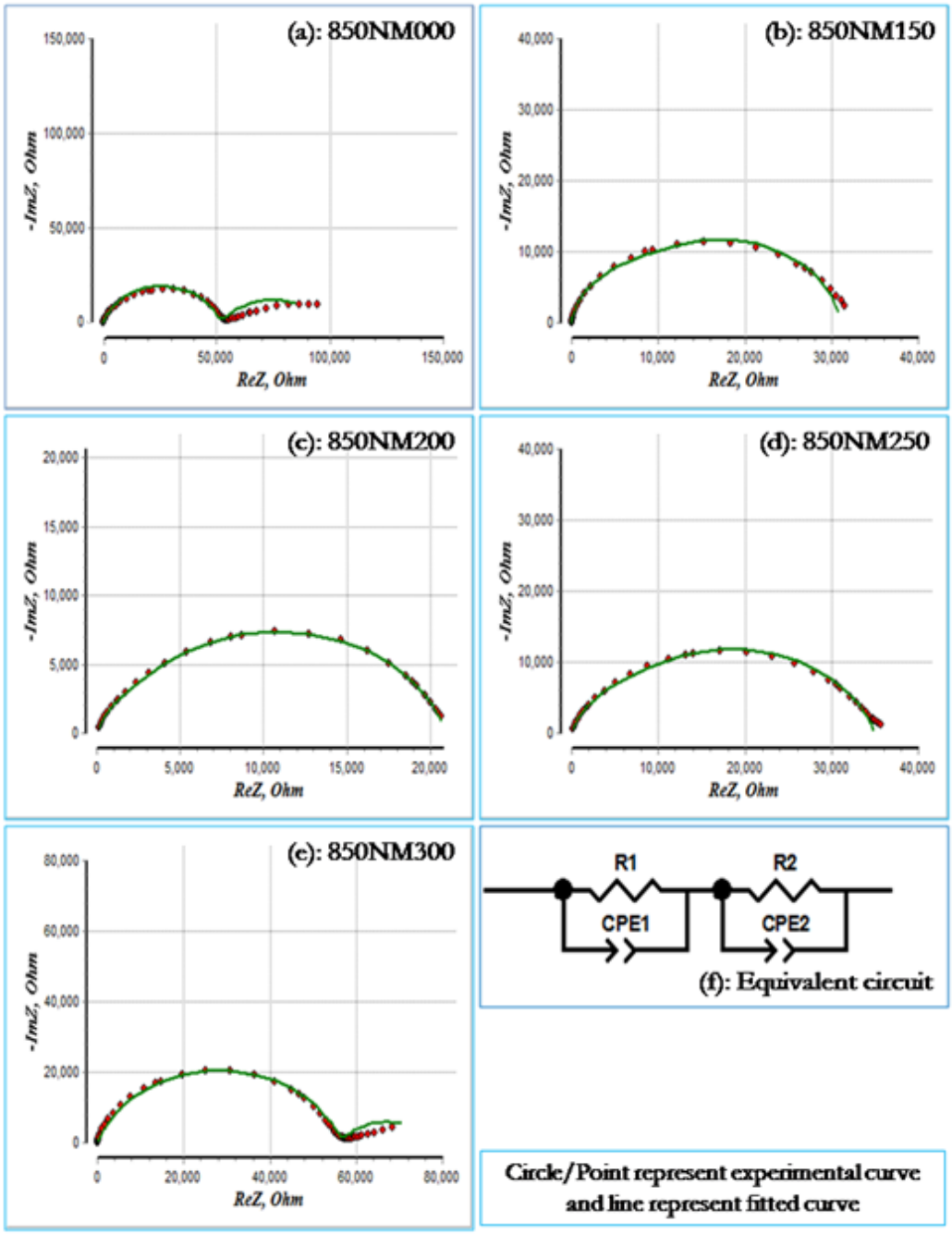

Figure 6.24: Experimental plots, fitted plots and equivalent circuit for fitting of impedance spectra of the samples as a function of MnO amount measured at 250°C : (a) 850NM000 (0.00 mol% MnO); (b) 850NM150 (1.50 mol% MnO); (c) 850NM200 (2.00 mol% MnO); (d) 850NM250 (2.50 mol% MnO); (e) 850NM300 (3.00 mol% MnO) and (f) equivalent circuit.

To understand the influence of the microstructure and the potential barrier on the electrical properties of ZnO ceramics, the impedance spectra of ZnO pellets were fitted with the electrical equivalent circuit (Figs. 6.22 to 6.30 (f)). The proposed electrical model consists of parallel distributed capacitance represented by resistance R and P (constant phase element). The results of the numerical equivalent circuit parameters fitting of plots using commercially available electrochemical impedance spectroscopy (EIS) [Bondarenko et al. (2005)] for all investigated structures are given in Table 6.10 to 6.18. The order of magnitude of the 'P' suggests that the semicircle is due to grain boundaries, typically of a double-layer effect [Jonscher (1977); Jorcin et al. (2006)]. In Figs. 6.22 to 6.30 (f), R_1 and P_1 denote the resistance, and capacitance/CPE is assigned to the high-frequency defects and/or adsorbed species at the grain boundary region, not necessarily at the same grain boundary; R_2 and P_2 represent the resistance and capacitance/CPE of the low-frequency grain boundary of most resistive elements that dominate the impedance results. The two R-values obtained at 50 °C, 150 °C & 250 °C are given from Tables 6.10 to 6.18 and were obtained by plot fitting. These values were further used to evaluate the apparent activation energy for charge transport through the grain boundary.

Figs. 6.22, 6.23, 6.24 and Tables 6.10, 6.11, 6.12 shows the total resistance given by R_T (Ω) = R_1 (Ω) + R_2 (Ω) of the samples sintered at 850 °C with different amounts of MnO measured at 50°C, 150°C & 250°C respectively. The R_T (Ω) for the 0.00 mol%, 1.50 mol%, 2.00 mol%, 2.50 mol% and 3.00 mol% MnO doped ZnO-V_2O_5-Nb_2O_5 samples measured at 50 °C are $3.70x10^8$, $9.88x10^7$, $8.33x10^7$, $2.19x10^8$, $1.51x10^8$; at 150 °C are $5.71x10^6$, $1.98x10^6$, $1.14x10^6$, $3.00x10^6$, $2.68x10^6$ and at 250 °C are $1.29x10^5$, $3.10x10^4$, $2.18x10^4$, $3.50x10^4$, $7.68x10^4$ (Ω) respectively.

Table 6.10: Summary of fitted electrical parameter obtained from EIS software for MnO doped ZnO-V_2O_5-Nb_2O_5 materials sintered at 850 °C and measured at 50 °C.

Samples (at 50°C)	$R_1(\Omega)$	P_1	n_1	$R_2(\Omega)$	P_2	n_2	$R_T(\Omega)$
850NM000	$1.54x10^8$	$2.13x10^{-9}$	0.72	$2.16x10^8$	$4.96x10^{-8}$	0.53	$3.70x10^8$
850NM150	$2.09x10^7$	$3.08x10^{-7}$	0.90	$7.79x10^7$	$4.82x10^{-9}$	0.69	$9.88x10^7$
850NM200	$1.27x10^7$	$1.29x10^{-9}$	0.99	$7.07x10^7$	$2.93x10^{-9}$	0.83	$8.33x10^7$
850NM250	$2.01x10^7$	$1.68x10^{-9}$	0.85	$1.99x10^8$	$2.98x10^{-9}$	0.88	$2.19x10^8$
850NM300	$2.80x10^7$	$1.21x10^{-6}$	0.91	$1.23x10^8$	$5.85x10^{-9}$	0.61	$1.51x10^8$

Table 6.11: Summary of fitted electrical parameter obtained from EIS software for MnO doped ZnO-V_2O_5-Nb_2O_5 materials sintered at 850 °C and measured at 150 °C.

Samples (at 150°C)	$R_1(\Omega)$	P_1	n_1	$R_2(\Omega)$	P_2	n_2	$R_T(\Omega)$
850NM000	$2.63\ x10^6$	$4.05x10^{-6}$	0.67	$3.08\ x10^6$	$3.53x10^{-9}$	0.72	$5.71\ x10^6$
850NM150	$4.34\ x10^5$	$1.43x10^{-9}$	0.96	$1.54\ x10^6$	$3.69x10^{-9}$	0.93	$1.98\ x10^6$
850NM200	$2.64\ x10^5$	$2.49x10^{-9}$	0.95	$8.80\ x10^5$	$5.23x10^{-9}$	0.82	$1.14\ x10^6$
850NM250	$2.88\ x10^5$	$1.43x10^{-9}$	0.91	$2.71\ x10^6$	$3.55x10^{-9}$	0.84	$3.00\ x10^6$
850NM300	$6.60\ x10^5$	$9.5x10^{-10}$	0.95	$2.02\ x10^6$	$3.68x10^{-9}$	0.90	$2.68\ x10^6$

Table 6.12: Summary of fitted electrical parameter obtained from EIS software for MnO doped ZnO-V_2O_5-Nb_2O_5 materials sintered at 850 °C and measured at 250 °C.

Samples (at 250°C)	$R_1(\Omega)$	P_1	n_1	$R_2(\Omega)$	P_2	n_2	$R_T(\Omega)$
850NM000	$7.60x10^4$	$1.70x10^{-5}$	0.55	$5.30x10^4$	$5.56x10^{-9}$	0.77	$1.29x10^5$
850NM150	$7.71x10^3$	$1.98x10^{-9}$	0.96	$2.33x10^4$	$5.18x10^{-9}$	0.92	$3.10x10^4$
850NM200	$2.17x10^3$	$5.32x10^{-9}$	0.91	$1.96x10^4$	$9.97x10^{-9}$	0.81	$2.18x10^4$
850NM250	$4.35x10^3$	$2.94x10^{-9}$	0.90	$3.07x10^4$	$8.31x10^{-9}$	0.80	$3.50x10^4$
850NM300	$2.26x10^4$	$4.11x10^{-5}$	0.56	$5.42x10^4$	$2.23x10^{-9}$	0.88	$7.68x10^4$

The total resistance R_T (Ω) measured at 50 °C for the sample doped with 0.00 mol% MnO is the maximum because of the small grain size; i.e., there are large number of grain boundaries.

Figs. 6.25, 6.26, 6.27 and Tables 6.13, 6.14, 6.15 shows the total resistance given by R_T (Ω) = R_1 (Ω) + R_2 (Ω) of the samples sintered at 900 °C with different amounts of MnO measured and calculated at 50 °C, 150 °C & 250 °C. The R_T (Ω) for the 0.00 mol%, 1.50 mol%, 2.00 mol%, 2.50 mol% and 3.00 mol% MnO doped ZnO-V_2O_5-Nb_2O_5 samples measured at 50 °C are 2.53 x10^8, 1.61 x10^8, 2.97 x10^8, 1.83 x10^8, 6.33 x10^7; at 150 °C are 5.24 x10^6, 3.16 x10^6, 1.56 x10^6, 2.30 x10^6, 7.01 x10^5 and at 250 °C are 5.28 x10^4, 6.87 x10^4, 3.98 x10^4, 4.67 x10^4, 1.40 x10^4 respectively. The resistivity of a polycrystalline material decreases with the increase in grain size due to the decrease in the grain boundary number. Therefore, we found that the 2.00 mol% MnO containing sample has a higher value of resistance among all the samples sintered at 900 °C.

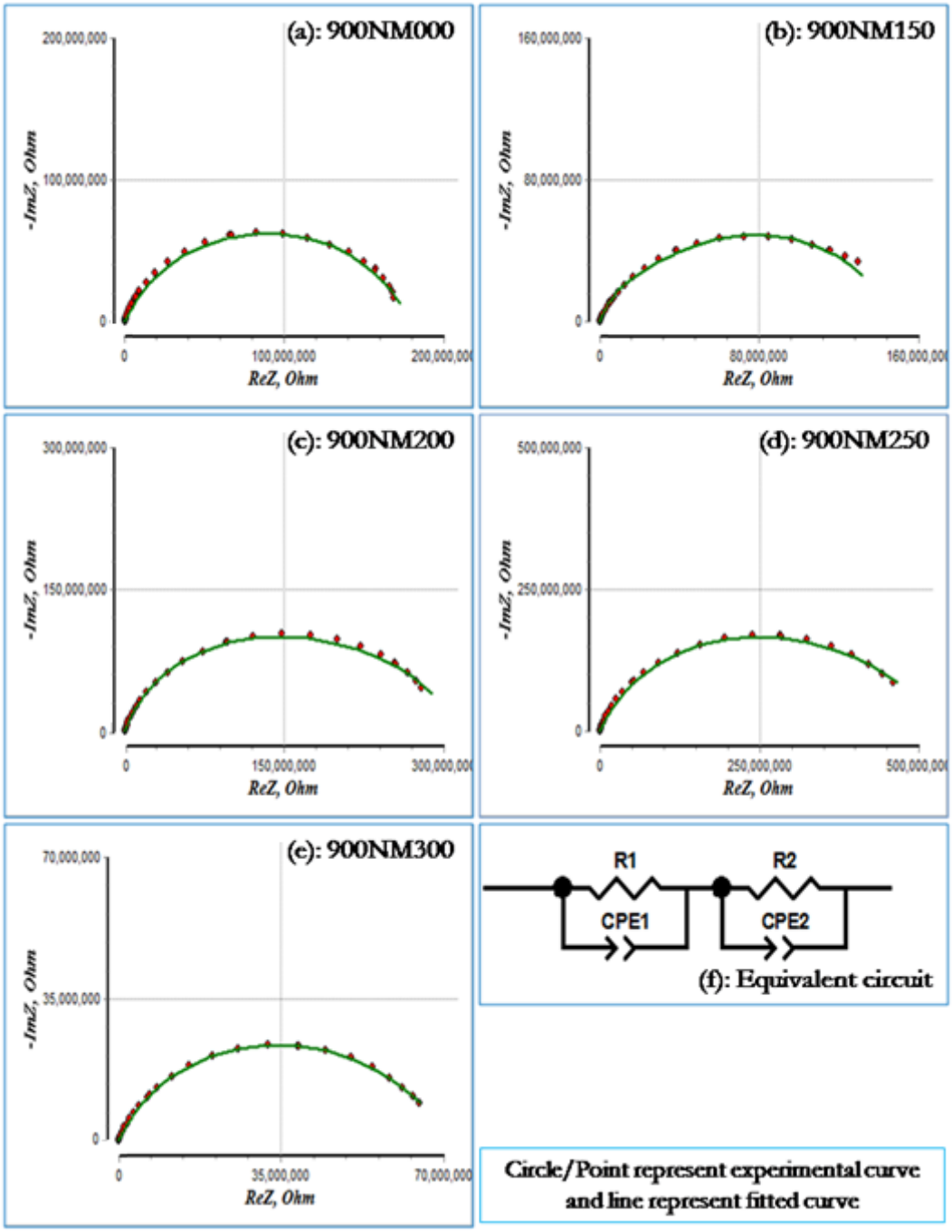

Figure 6.25: Experimental plots, fitted plots and equivalent circuit for fitting of impedance spectra of the samples as a function of MnO amount measured at 50 °C: (a) 900NM000 (0.00 mol% MnO); (b) 900NM150 (1.50 mol% MnO); (c) 900NM200 (2.00 mol% MnO); (d) 900NM250 (2.50 mol% MnO); (e) 900NM300 (3.00 mol% MnO) & (f) equivalent circuit.

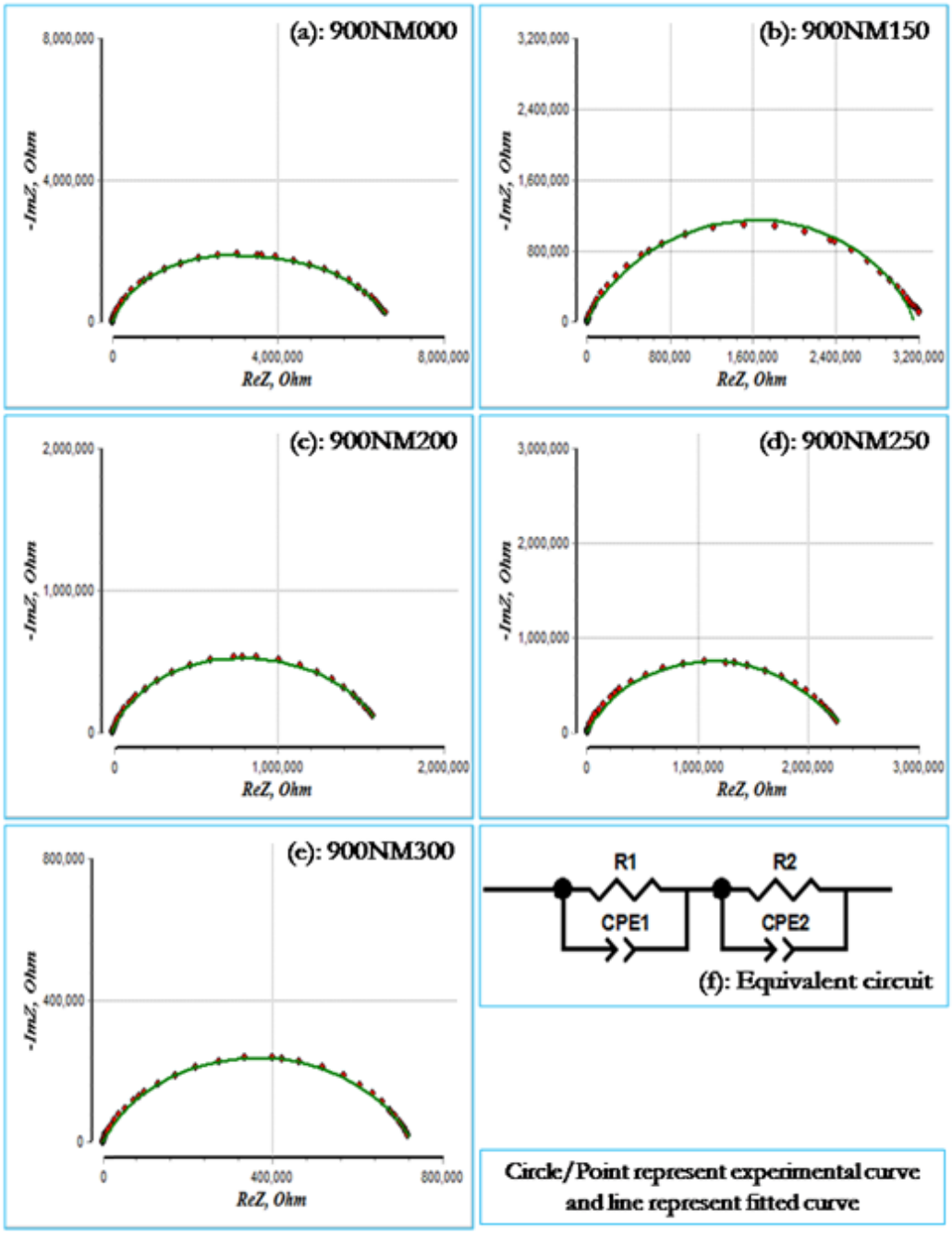

Figure 6.26 Experimental plots, fitted plots and equivalent circuit for fitting of impedance spectra of the samples as a function of MnO amount measured at 150 °C: (a) 900NM000 (0.00 mol% MnO); (b) 900NM150 (1.50 mol% MnO); (c) 900NM200 (2.00 mol% MnO); (d) 900NM250 (2.50 mol% MnO); (e) 900NM300 (3.00 mol% MnO) and (f) equivalent circuit.

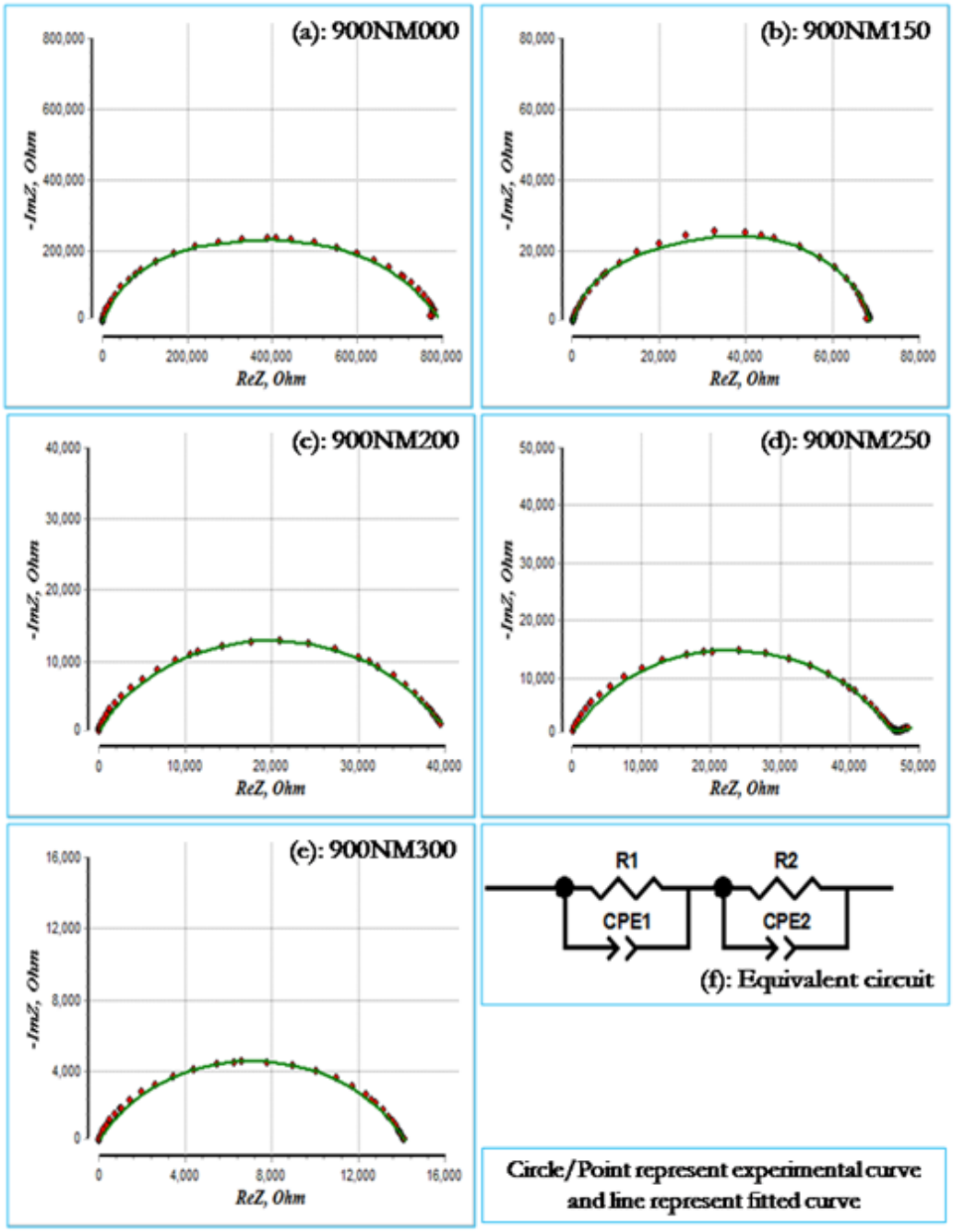

Figure 6.27: Experimental plots, fitted plots and equivalent circuit for fitting of impedance spectra of the samples as a function of MnO amount measured at 250 °C: (a) 900NM000 (0.00 mol% MnO); (b) 900NM150 (1.50 mol% MnO); (c) 900NM200 (2.00 mol% MnO); (d) 900NM250 (2.50 mol% MnO); (e) 900NM300 (3.00 mol% MnO) and (f) equivalent circuit.

Table 6.13: Summary of fitted electrical parameter obtained from EIS software measured at 50 °C for MnO doped ZnO-V_2O_5-Nb_2O_5 samples sintered at 900 °C.

Samples (at 50°C)	R_1 (Ω)	P_1	n_1	R_2 (Ω)	P_2	n_2	R_T (Ω)
900NM000	$4.15x10^7$	$1.88x10^{-9}$	0.93	$2.11x10^8$	$3.80x10^{-9}$	0.91	$2.53x10^8$
900NM150	$3.55x10^7$	$2.30x10^{-9}$	0.92	$1.26x10^8$	$3.95x10^{-9}$	0.89	$1.61x10^8$
900NM200	$8.80x10^7$	$9.4x10^{-10}$	0.96	$2.09x10^8$	$2.05x10^{-9}$	0.91	$2.97x10^8$
900NM250	$7.23x10^7$	$5.9x10^{-10}$	0.92	$4.29x10^8$	$9.1x10^{-10}$	0.91	$5.01x10^8$
900NM300	$3.26x10^6$	$2.36x10^{-9}$	0.92	$6.00x10^7$	$2.39x10^{-9}$	0.88	$6.33x10^7$

Table 6.14: Summary of fitted electrical parameter obtained from EIS software measured at 150 °C for MnO doped ZnO-V_2O_5-Nb_2O_5 samples sintered at 900 °C.

Samples (at 150°C)	R_1 (Ω)	P_1	n_1	R_2 (Ω)	P_2	n_2	R_T (Ω)
900NM000	$6.34x10^5$	$1.32x10^{-9}$	0.95	$4.60x10^6$	$5.27x10^{-9}$	0.93	$5.24\ x10^6$
900NM150	$1.20x10^6$	$2.42x10^{-9}$	0.90	$1.96x10^6$	$9.58x10^{-9}$	0.91	$3.16\ x10^6$
900NM200	$2.58x10^5$	$1.56x10^{-9}$	0.92	$1.31x10^6$	$3.28x10^{-9}$	0.89	$1.56\ x10^6$
900NM250	$4.83x10^5$	$5.39\ x10^{-8}$	0.65	$1.82x10^6$	$2.41x10^{-9}$	0.78	$2.30\ x10^6$
900NM300	$9.03x10^4$	$2.27x10^{-9}$	0.92	$6.10x10^5$	$4.76x10^{-9}$	0.88	$7.01\ x10^5$

Table 6.15: Summary of fitted electrical parameter obtained from EIS software measured at 250 °C for MnO doped ZnO-V_2O_5-Nb_2O_5 samples sintered at 900 °C.

Samples (at 250°C)	R_1 (Ω)	P_1	n_1	R_2 (Ω)	P_2	n_2	R_T (Ω)
900NM000	$1.33x10^4$	$1.98x10^{-9}$	0.96	$3.96x10^4$	$6.56x10^{-9}$	0.91	$5.28\ x10^4$
900NM150	$2.17x10^4$	$3.47x10^{-9}$	0.92	$4.70x10^4$	$9.87x10^{-9}$	0.89	$6.87\ x10^4$
900NM200	$1.36x10^4$	$3.93x10^{-9}$	0.87	$2.62x10^4$	$2.12\ x10^{-8}$	0.80	$3.98\ x10^4$
900NM250	$1.24x10^4$	$1.56x10^{-9}$	0.89	$3.43x10^4$	$8.91x10^{-9}$	0.81	$4.67\ x10^4$
900NM300	$2.30x10^3$	$2.58x10^{-9}$	0.94	$1.17x10^4$	$1.39x10^{-8}$	0.83	$1.40\ x10^4$

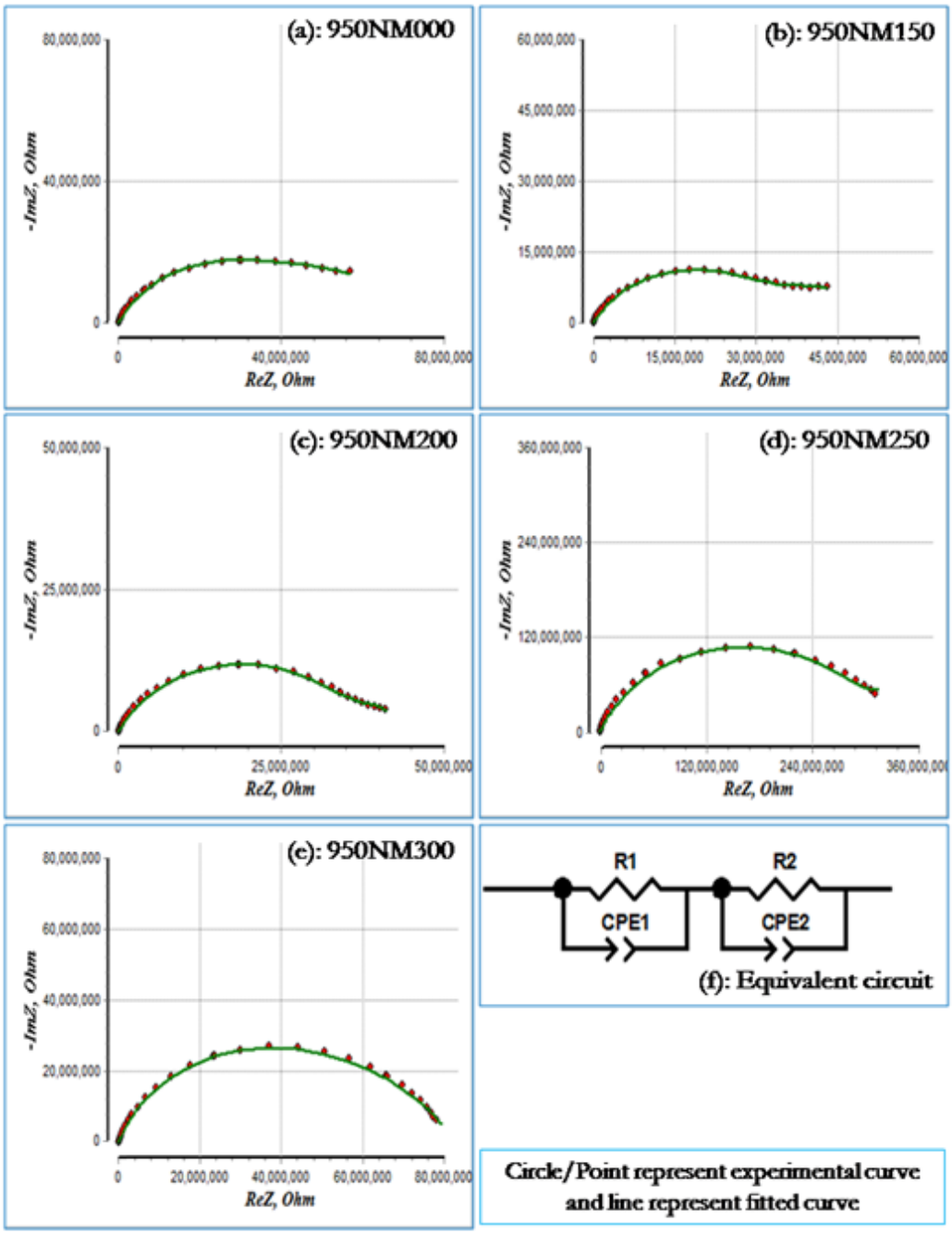

Figure 6.28: Experimental plots, fitted plots and equivalent circuit for fitting of impedance spectra of the samples as a function of MnO amount measured at 50 °C: (a) 950NM000 (0.00 mol% MnO); (b) 950NM150 (1.50 mol% MnO); (c) 950NM200 (2.00 mol% MnO); (d) 950NM250 (2.50 mol% MnO); (e) 950NM300 (3.00 mol% MnO) and (f) equivalent circuit.

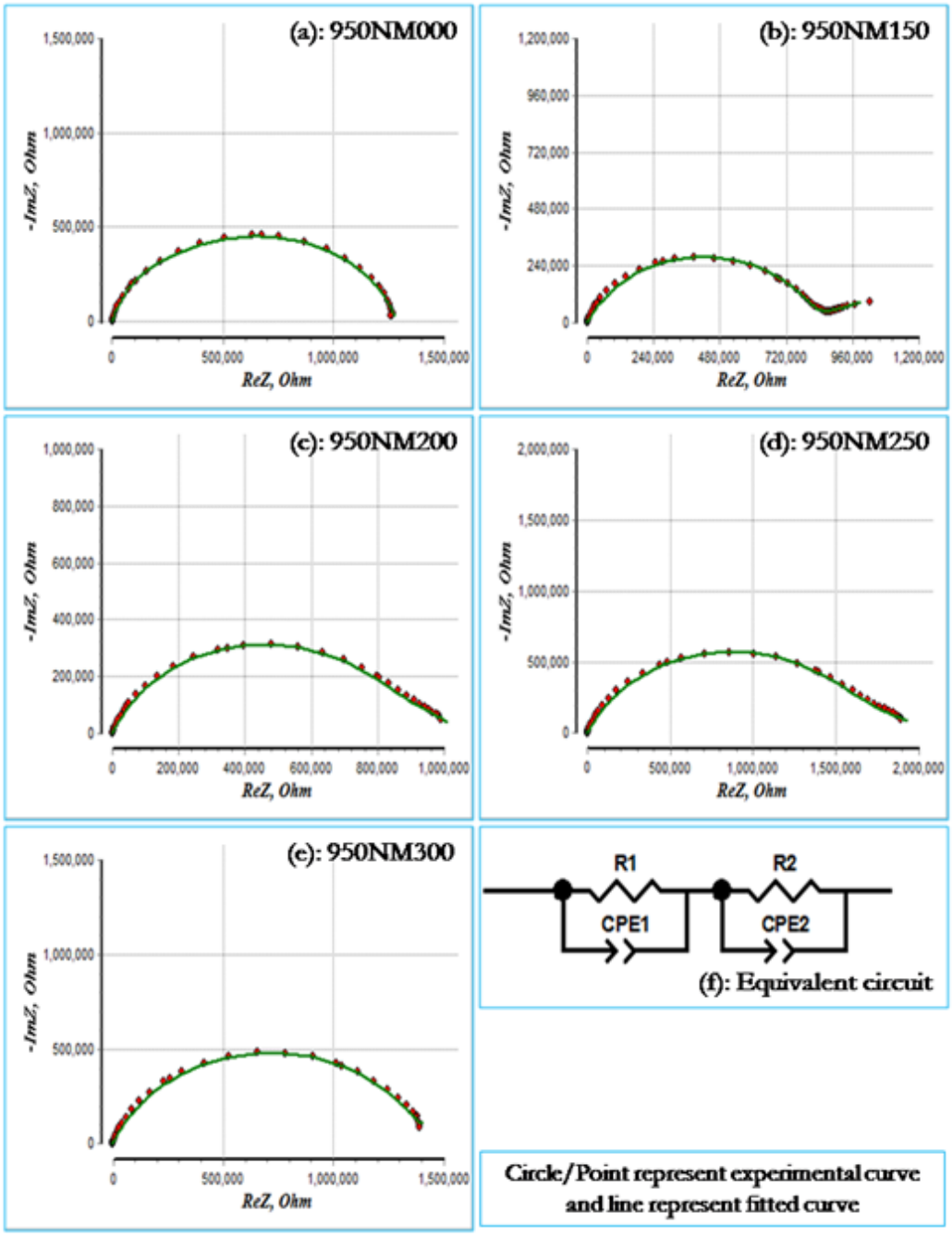

Figure 6.29: Experimental plots, fitted plots and equivalent circuit for fitting of impedance spectra of the samples as a function of MnO amount measured at 150 °C: (a) 950NM000 (0.00 mol% MnO); (b) 950NM150 (1.50 mol% MnO); (c) 950NM200 (2.00 mol% MnO); (d) 950NM250 (2.50 mol% MnO); (e) 950NM300 (3.00 mol% MnO) and (f) equivalent circuit.

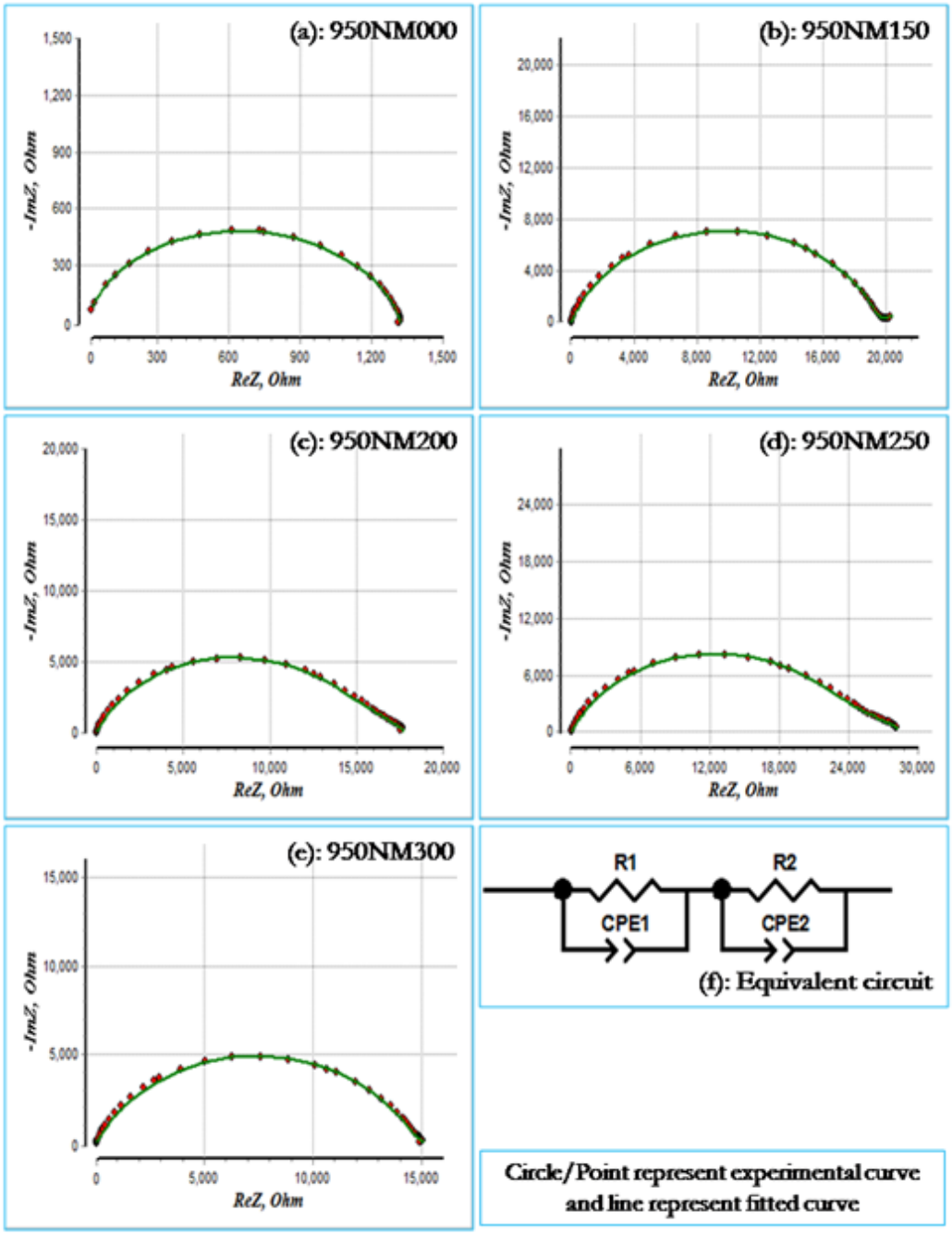

Figure 6.30: Experimental plots, fitted plots and equivalent circuit for fitting of impedance spectra of the samples as a function of MnO amount measured at 50 °C: (a) 950NM000 (0.00 mol% MnO); (b) 950NM150 (1.50 mol% MnO); (c) 950NM200 (2.00 mol% MnO); (d) 950NM250 (2.50 mol% MnO); (e) 950NM300 (3.00 mol% MnO) and (f) equivalent circuit.

Table 6.16: Summary of fitted electrical parameter obtained from EIS software measured at 50 °C for MnO doped ZnO-V_2O_5-Nb_2O_5 samples sintered at 950 °C.

Samples (at 50°C)	$R_1(\Omega)$	P_1	n_1	$R_2(\Omega)$	P_2	n_2	$R_T(\Omega)$
950NM000	$8.29x10^6$	$1.80x10^{-9}$	0.92	$4.54x10^7$	$4.23x10^{-9}$	0.90	$5.36\ x10^7$
950NM150	$1.26x10^7$	$3.58x10^{-9}$	0.93	$5.01x10^7$	$1.20x10^{-8}$	0.90	$6.27\ x10^7$
950NM200	$6.01x10^6$	$4.23x10^{-9}$	0.89	$3.12x10^7$	$8.51x10^{-9}$	0.86	$3.72\ x10^7$
950NM250	$7.14x10^7$	$1.62x10^{-9}$	0.92	$2.22x10^8$	$4.11x10^{-9}$	1.00	$2.93\ x10^8$
950NM300	$8.35x10^6$	$5.24x10^{-9}$	0.91	$7.32x10^7$	$6.44x10^{-9}$	0.90	$8.16\ x10^7$

Table 6.17: Summary of fitted electrical parameter obtained from EIS software measured at 150 °C for MnO doped ZnO-V_2O_5-Nb_2O_5 samples sintered at 950 °C.

Samples (at 150°C)	$R_1(\Omega)$	P_1	n_1	$R_2(\Omega)$	P_2	n_2	$R_T(\Omega)$
950NM000	$2.27x10^5$	$1.36x10^{-9}$	0.96	$1.01x10^6$	$2.63x10^{-9}$	0.94	$1.24\ x10^6$
950NM150	$1.31x10^5$	$4.07x10^{-9}$	0.95	$6.67x10^5$	$8.47x10^{-9}$	0.93	$7.98\ x10^5$
950NM200	$1.50x10^5$	$4.49x10^{-9}$	0.92	$7.81x10^5$	$8.42x10^{-9}$	0.89	$9.31\ x10^5$
950NM250	$3.40x10^5$	$2.57x10^{-9}$	0.93	$1.41x10^6$	$6.80x10^{-9}$	0.90	$1.75\ x10^6$
950NM300	$1.27x10^5$	$6.12x10^{-9}$	0.93	$1.22x10^6$	$8.42x10^{-9}$	0.90	$1.34\ x10^6$

Table 6.18: Summary of fitted electrical parameter obtained from EIS software measured at 250 °C for MnO doped ZnO-V_2O_5-Nb_2O_5 samples sintered at 950 °C.

Samples (at 250°C)	$R_1(\Omega)$	P_1	n_1	$R_2(\Omega)$	P_2	n_2	$R_T(\Omega)$
950NM000	$2.96x10^2$	$2.24x10^{-9}$	1.00	$1.03x10^3$	$2.51\ x10^{-8}$	0.80	$1.33\ x10^3$
950NM150	$2.94x10^3$	$3.94x10^{-9}$	0.99	$1.65x10^4$	$1.05\ x10^{-8}$	0.92	$1.95\ x10^4$
950NM200	$5.39x10^3$	$6.50x10^{-9}$	0.91	$1.16x10^4$	$4.40\ x10^{-8}$	0.83	$1.70\ x10^4$
950NM250	$8.64x10^3$	$5.45x10^{-9}$	0.90	$1.81x10^4$	$3.70\ x10^{-8}$	0.83	$2.67\ x10^4$
950NM300	$2.55x10^3$	$1.40x10^{-5}$	0.60	$1.28x10^4$	$1.33\ x10^{-8}$	0.87	$1.53\ x10^4$

Figs. 6.28, 6.29, 6.30 and Tables 6.16, 6.17 & 6.18 shows the total resistance given by $R_T\ (\Omega) = R_1\ (\Omega) + R_2\ (\Omega)$ measured at 50 °C, 150 °C & 250 °C of the samples sintered at 950 °C with different amounts of MnO. The $R_T\ (\Omega)$ for the 0.00 mol%, 1.50 mol%, 2.00 mol%, 2.50 mol% and 3.00 mol% MnO doped ZnO-V_2O_5-Nb_2O_5 samples measured at 50 °C are 5.36 $x10^7$, 6.27 $x10^7$, 3.72 $x10^7$, 2.93

$x10^8$, 8.16 $x10^7$; at 150 °C are 1.24 $x10^6$, 7.98 $x10^5$, 9.31 $x10^5$, 1.75 $x10^6$, 1.34 $x10^6$ and at 250 °C are 1.33 $x10^3$, 1.95 $x10^4$, 1.70 $x10^4$, 2.67 $x10^4$, 1.53 $x10^4$ respectively. The 2.50 mol% MnO containing samples sintered at 950 °C have a higher value of resistance among all the samples sintered at 950 °C. Since, the resistivity of a polycrystalline material decreases with the increase in grain size and the decrease in the grain boundary number.

Figs. 6.31, 6.32 and 6.33 (a-e) present the Arrhenius plots of the R_1 and R_2 regions for high and low frequencies respectively. These figures show the presence of two linear regions with different slopes. The slope change in the two cases occured at ~150 °C/200 °C. Table 6.19, 6.20 and 6.21 presents the activation energies for the two processes as a function of MnO doped samples calculated from the data presented in Figs. 6.31, 6.32 and 6.33. The resistance data in both R_1 and R_2 regions follow the Arrhenius law [Pandey et al. (2007)]

$$R = R_0 \exp\left(-\frac{E_a}{RT}\right) \tag{6.4}$$

where E_a is the activation energy for conduction, k_B is the Boltzmann's constant and R_0 is the pre-exponential factor. The least square fitting method of the resistance data were used to calculate the activation energies 'Ea' of conduction. The temperature dependence of the R_1 and R_2 regions shows considerable complexity.

Fig. 6.31 shows the curvature in the Arrhenius plots and activation energy of 0.389 to 0.516 eV below approximately 150°C/200°C. Above 150 °C/200 °C, the activation energies were found in the range of 0.714 to 0.852 eV, this is because of the varistor action is critically dependent on the presence of excess oxygen (as well as V) at ZnO-ZnO interfaces and the activation energies with varying temperature. The level of 0.389 to 0.516 eV is related to the charge state of interstitial oxygen $O_i^{-1}$and O_i^0. Form Table 6.19, for the 0.00 mol%, 1.50 mol%, 2.00 mol%, 2.50 mol% and 3.00 mol% MnO-doped sample sintered at 850 °C for 3 h, the Ea values are 0.410, 0.448, 0.458, 0.498, 0.428 eV for R_1 and 0.389, 0.458, 0.516, 0.512, 0.487 eV for R_2 grain boundaries regions respectively. In relation to the nature of the interface states, two types of grain boundary junctions have

been suggested, ZnO–ZnO homojunction (0.389 to 0.516 eV) and ZnO-V_2O_5-ZnO heterojunction (0.714 to 0.852 eV), as defined by impedance spectroscopy [West et al. (1997)]. It is quite possible that the compositions of the V rich intergranular phases responsible for the interface states in ZnO varistors are varied with doping constituents and heat-treatment conditions [Chen et al. (2015); Wu et al. (2011)]. Consequently, it is reasonable to assign an energy level 0.389 to 0.516 eV to the interface state of ZnO-intergranular phase heterojunction modified by Mn [Nahm et al. (2007); (2009); (2011); (2015)].

Fig. 6.32 shows the curvature in the Arrhenius plots and activation energy of 0.445 to 0.680 eV below approximately 150 °C/200 °C. Above 150 °C/200 °C, the activation energies were in the range of 0.722 to 0.973 eV, this is because of the varistor action is critically dependent on the presence of excess oxygen (as well as V) at ZnO-ZnO interfaces and the activation energies with varying temperature. The level 0.445 to 0.680 eV is related to the charge state of interstitial oxygen $O_i^{-1}$and O_i^0. Form Table 6.20, for the 0.00 mol%, 1.50 mol%, 2.00 mol%, 2.50 mol% and 3.00 mol% MnO-doped sample sintered at 900°C for 3 h, the Ea values below 150°C/200°C for R_1 are 0.485, 0.486, 0.670, 0.614, 0.480 eV and 0.445, 0.544, 0.617, 0.680, 0.587 eV for R_2 grain boundaries regions respectively. In relation to the nature of the interface states, two types of grain boundary junctions have been suggested that is ZnO–ZnO homojunction (0.445 to 0.680 eV) and ZnO-V_2O_5-ZnO heterojunction (0.722 to 0.973 eV), as defined by impedance spectroscopy [West et al. (1997)]. It is quite possible that the compositions of the V-rich intergranular phases responsible for the interface states in ZnO varistors are varied with doping constituents and heat-treatment conditions. Consequently, it is reasonable to assign an energy level 0.445 to 0.680 eV to the interface state of ZnO intergranular phase heterojunction modified by Mn [Nahm et al. (2007); (2009); (2011); (2015)].

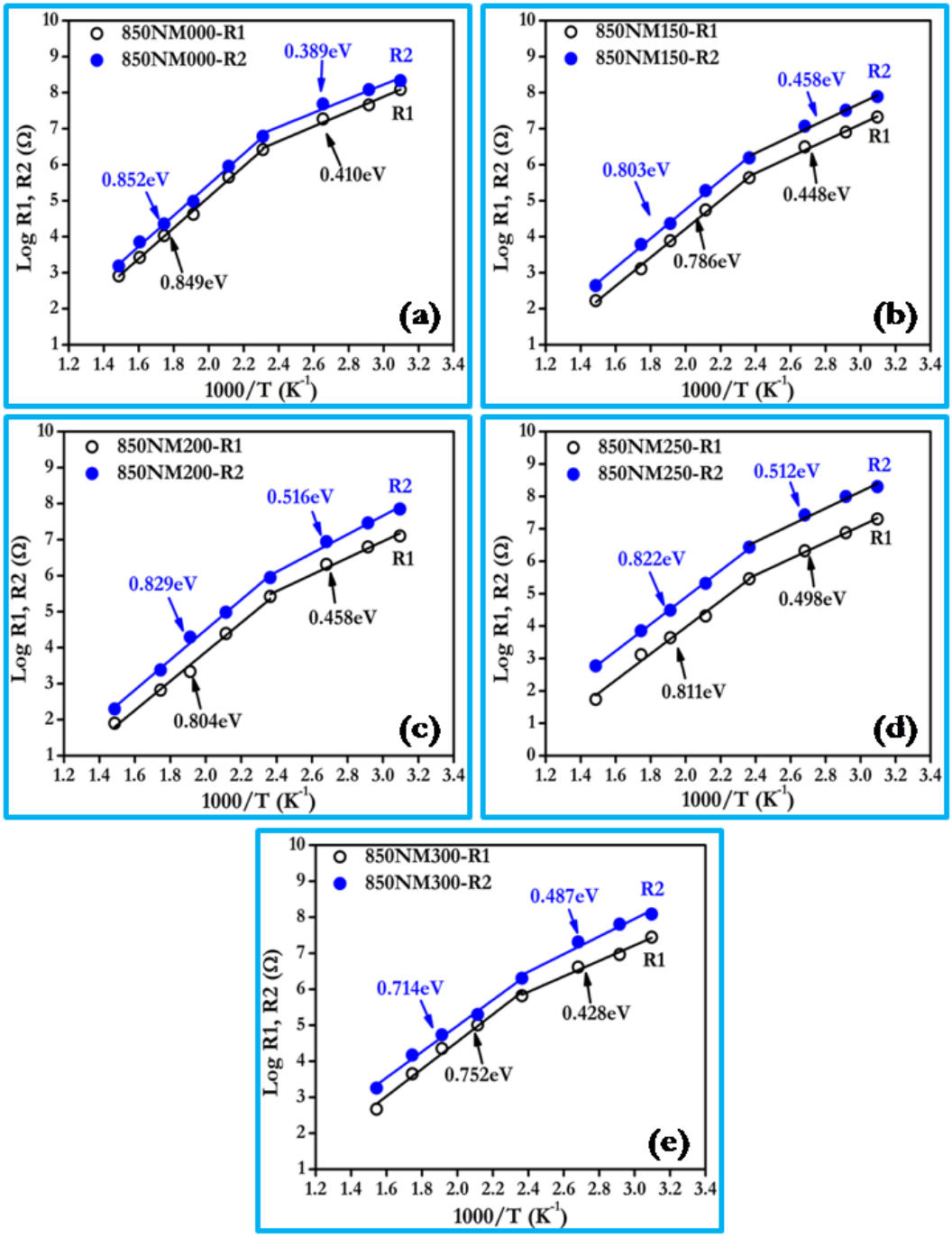

Figure 6.31: Arrhenius plots for resistance R_1 and R_2 associated with low and high frequency grain boundary respectively of the samples as a function of MnO amount: (a) 850NM000 (0.00 mol% MnO); (b) 850NM150 (1.50 mol% MnO); (c) 850NM200 (2.00 mol% MnO); (d) 850NM250 (2.50 mol% MnO) and (e) 850NM300 (3.00 mol% MnO).

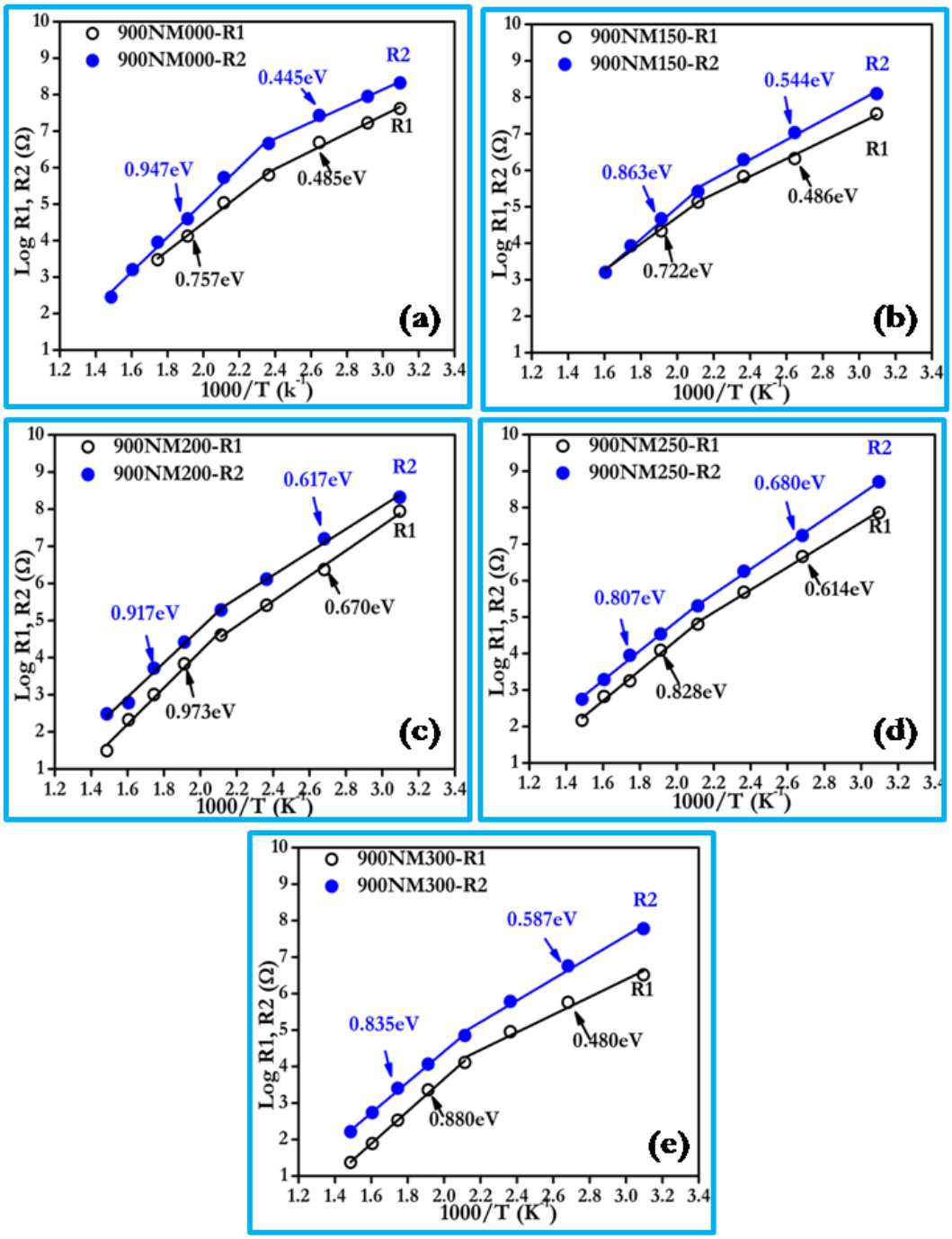

Figure 6.32: Arrhenius plots for resistance R_1 and R_2 associated with low and high frequency grain boundary respectively of the samples as a function of MnO amount: (a) 900NM000 (0.00 mol% MnO); (b) 900NM150 (1.50 mol% MnO); (c) 900NM200 (2.00 mol% MnO); (d) 900NM250 (2.50 mol% MnO) and (e) 900NM300 (3.00 mol% MnO).

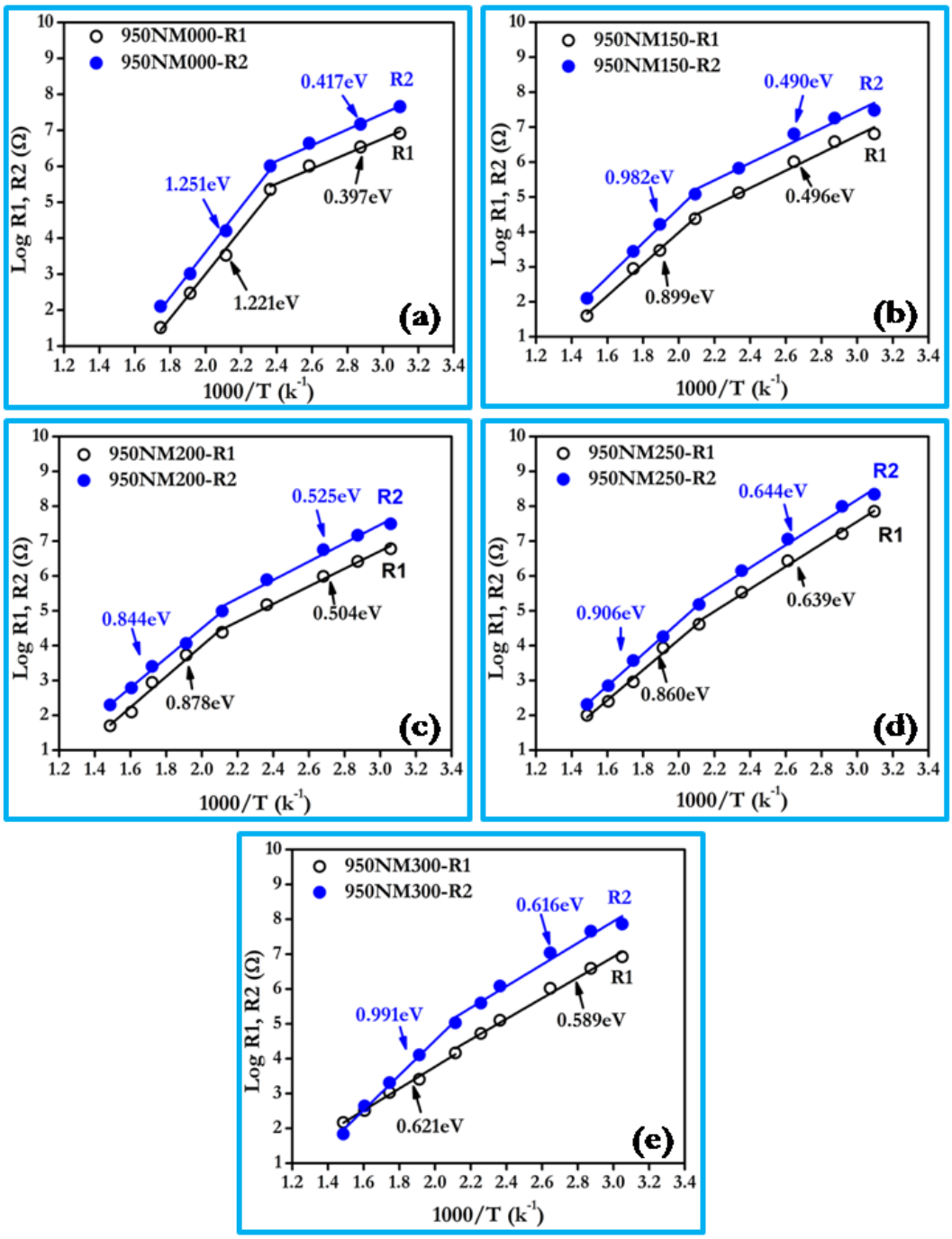

Figure 6.33: Arrhenius plots for resistance R_1 and R_2 associated with low and high frequency grain boundary respectively of the samples as a function of MnO amount: (a) 950NM000 (0.00 mol% MnO); (b) 950NM150 (1.50 mol% MnO); (c) 950NM200 (2.00 mol% MnO); (d) 950NM250 (2.50 mol% MnO) and (e) 950NM300 (3.00 mol% MnO)

Fig. 6.33 shows the curvature in the Arrhenius plots and activation energy of 0.397 to 0.644 eV below approximately 150 °C/200 °C. Above 150 °C/200 °C, the activation energies were in the range of 0.621 to 1.251 eV, this is because of the varistor action is critically dependent on the presence of excess oxygen (as well as V) at ZnO-ZnO interfaces and the activation energies with varying temperature. The level of 0.397 to 0.644 eV is related to the charge state of interstitial oxygen $O_i^{-1}$and O_i^0. Form Table 6.21, for the 0.00 mol%, 1.50 mol%, 2.00 mol%, 2.50 mol% and 3.00 mol% MnO-doped sample sintered at 950°C for 3 h, the Ea values below 150°C/200°C are 0.397, 0.496, 0.504, 0.639, 0.589 eV for R_1 and 0.417, 0.490, 0.525, 0.644, 0.616 eV for R_2 grain boundaries regions respectively. In relation to the nature of the interface states, two types of grain boundary junctions have been suggested that is ZnO–ZnO homojunction (0.397 to 0.644 eV) and ZnO-V_2O_5-ZnO heterojunction (0.621 to 1.251 eV), as defined by impedance spectroscopy [West et al. (1997)]. It is quite possible that the compositions of the V-rich intergranular phases responsible for the interface states in ZnO varistors are varied with doping constituents and heat-treatment conditions [Chen et al. (2015); Wu et al. (2011)]. Consequently, it is reasonable to assign an energy level of 0.397 to 0.644 eV to the interface state of ZnO intergranular phase heterojunction modified by Mn [Nahm et al. (2007); (2009); (2011); (2015)].

Table 6.19: Activation energies calculated from the Arrhenius plot at low and high frequency region for the temperature range below and above 150 °C for the samples sintered at 850 °C.

Samples	R_1 : E_1: (eV)		R_2 : E_2: (eV)	
	T<150 °C	T>150 °C	T<150 °C	T>150 °C
850NM000	0.410	0.849	0.389	0.852
850NM150	0.448	0.786	0.458	0.803
850NM200	0.458	0.804	0.516	0.829
850NM250	0.498	0.811	0.512	0.822
850NM300	0.428	0.752	0.487	0.714

Table 6.20: Activation energies calculated from the Arrhenius plot at low and high frequency region for the temperature range below and above 150°C/200°C for the samples sintered at 900 °C.

Samples	R_1 : E_1: (eV)		R_2 : E_2: (eV)	
	T<150 °C	T>150 °C	T<150 °C	T>150 °C
900NM000	0.485	0.757	0.445	0.947
	T<200 °C	T>200 °C	T<200 °C	T>200 °C
900NM150	0.486	0.722	0.544	0.863
900NM200	0.670	0.973	0.617	0.917
900NM250	0.614	0.828	0.680	0.807
900NM300	0.480	0.880	0.587	0.835

Table 6.21: Activation energies calculated from the Arrhenius plot at low and high frequency region for the temperature range below and above 150°C/200°C for the samples sintered at 950 °C.

Samples	R_1 : E_1: (eV)		R_2 : E_2: (eV)	
	T<150 °C	T>150 °C	T<150 °C	T>150 °C
950NM000	0.397	1.221	0.417	1.251
	T<200 °C	T>200 °C	T<200 °C	T>200 °C
950NM150	0.496	0.899	0.49	0.982
950NM200	0.504	0.878	0.525	0.844
950NM250	0.639	0.86	0.644	0.906
950NM300	0.589	0.621	0.616	0.991

From Arrhenius plots, it has been observed that for the doping of MnO, the resistance of doped sample decreases and then increases as compared to the ZnO-V_2O_5-Nb_2O_5 systems for 850-950 ^oC sintering temperature. The effect of MnO on the electrical properties of ZnO based resistors can be commentated with grain boundary barrier model for ZnO based resistors. The defects generated by the presence of MnO as +2, +3 +4 are fundamental in the formation of depletion layers at the grain boundaries in that they lead to the creation of potential barriers when compensated by the negative charges at the grain boundary interface [Levinson (1979)].

ZnO is well known for its non-stoichiometry due to the zinc atoms interstitial sites and exhibits oxygen vacancies. These defects introduce donor states in the

forbidden band, slightly below the conducting band. The donors are assumed to be interstitial zinc ions Zn^{i}. Using Kroger–Vink notation, we can write:

$$Zn_i^x \rightarrow e' + Zn_i^0 \quad (6.5)$$

$$Zn_i^0 \rightarrow e' + Zn_i^{00} \quad (6.6)$$

where Zn_i^0 and Zn_i^{00} are once and twice ionized interstitial zinc atoms, respectively. Such free electrons (e') moves to the conducting band and enhances the ZnO conductivity which can be further increased by the extrinsic defects. But when ZnO is doped with V_2O_5, a part of the V_2O_5 additive have dissolved into the ZnO matrix and V^{5+} ions enter the interstitial sites of ZnO structure. Therefore, a substitutional reaction was believed to occur as below:

$$V_2O_5 \xrightarrow{ZnO} 2V_{Zn}^{000} + 2O_0 + \frac{3}{2}O_2 + 6e' \quad (6.7)$$

or

$$V_2O_5 \xrightarrow{ZnO} 2V_{Zn}^{000} + 2V_{Zn}^{2} + 5O_0 \quad (6.8)$$

Eq. (6.7) is an electron compensation reaction and the Eq. (6.8) is a defect compensation reaction. As there are more donors induced in ZnO–V_2O_5 than the intrinsic ones in ZnO, the electron compensation reaction seems more likely to have occurred. V_{Zn} is vanadium atom in zinc atom substitution site. In Zn substitutions with Vanadium atoms, free electrons are released and raise the conductivity by increasing electron density. Thus increase in conductivity was observed with increase in V_2O_5 content. Moreover, the zinc vacancies distribute preferably near the grain boundaries for a relaxation of the high strain induced by the vacancies. A schottky barrier might be induced by such a concentration gradient of defects created at the grain boundaries for the ZnO–V_2O_5 system. It should be mentioned that the barrier height depends on the applied voltage and vanishes above certain field strength. Also the barrier decreases with increase in grain conductivity and collapses when the grain conductivity is too high [Levinson (1979); Hng et al. (1999); (2000)].

From the Figs. 6.31, 6.32 and 6.33, it is observed that there is a decrease in resistance with increasing temperature. It could be attributed to negative temperature coefficient of resistance and semiconducting behavior of MnO doped ZnO-V_2O_5-Nb_2O_5 systems, obeying $R=R_0\, e^{-Ea/KT}$ in the temperature range of 50 to 400˚C. The resistance of Mn doped ZnO varistor falls suddenly in linear fashion up to certain transition temperature and after that the resistance decreases exponentially with increasing temperature. The transition temperature depends on doping concentration as well as sintering temperature.

From Arrhenius plots, it is observed that the curve for ZnO-V_2O_5-Nb_2O_5-MnO systems have low temperature region and high temperature region. The change in slope of the graph, from one region to other region occurs between two temperatures, depending upon the sintering temperature as well as the amount of MnO doping in ZnO-V_2O_5-Nb_2O_5 varistor. The transition temperatures for the MnO doping in ZnO-V_2O_5-Nb_2O_5 varistor with 0.00 mol%, 1.50 mol%, 2.00 mol%, 2.50 mol%, 3.00 mol% MnO-doped samples are 150˚C and 200˚C.

The values of E_a obtained correspond to typical hopping energy values between variable valence ions of the same dopant (Mn). Slightly higher values of activation energies for grain boundaries are due to more disordered nature of grain boundaries. Mn can exist in three variable valence states of +2, +3 and +4 depending on temperature of heat treatment. There may be larger concentration of Mn in variable valence states. [Pandey et al. (1997)]. During heating, the solubility of Mn^{+3} and Mn^{+4} ions were increased because of the lower ionic radii. As a result, more Mn ions were segregated in the grain boundaries and improved the non-linearity characteristics. Temperature behavior of the impedance data can be described as follows: For lower temperatures, the presence of $V_o^{\cdot\cdot}$ or $Zn_i^{\cdot\cdot}$ may be related with the low and high frequency time constants, respectively. Physically adsorbed water should be ruled out once the varistor system is dense. For higher temperatures, O’ and O” are the main adsorbed species at the grain boundary.

Summary: The present chapter discussed the influence of the MnO content on the structure and the electrical response of $ZnO–V_2O_5–Nb_2O_5$ based varistors ceramics was analysed using AC impedance spectroscopy. Samples were prepared via solid state reaction at different sintering temperature 850 °C, 900 °C & 950 °C. The microstructure of the MnO doped $ZnO–V_2O_5–Nb_2O_5$ varistors consisted of ZnO grain as the primary phase, ZnV_2O_4 and $Zn_3(VO_4)_2$ as the major secondary phases, in which $Zn_3(VO_4)_2$ acts as liquid-phase sintering promoter and has a significant effect on the sintered density. The average grain size of the MnO doped $ZnO–V_2O_5–Nb_2O_5$ system sintered from 850 to 950°C was found to be in range of 5.2 to 18.5 μm, which increases or decreases upon the amount of MnO addition. The MnO doped $ZnO–V_2O_5$- Nb_2O_5 sample sintered at 900°C exhibited the most optimum grain size of 8.4 μm. EDS spectra of ZnO grain boundary show V, Nb and Mn segregation in the samples. Among all of the samples, the 0.00 mol% MnO-doped sample sintered at 850 °C was found to have the highest values of total resistance of 370 MΩ. The 2.50 mol% MnO doped $ZnO–V_2O_5–Nb_2O_5$ system sintered at 900°C exhibited the highest nonlinear coefficient of 28.1, the highest breakdown field value of 572.6 V/mm, the lowest leakage current density of J_L = 51.204 μA/cm^2, the ε' (1KHz) = 312.1 and the tan δ(1KHz) = 0.152 among all of the samples. Ea values below 200 °C for 2.50 mol% MnO-doped samples sintered at 900 °C were found to be 0.614 and 0.680 eV for the R_1 (high frequency) and R_2 (low frequency) grain boundary regions, respectively. Conclusively, among all of the MnO doped $ZnO–V_2O_5–Nb_2O_5$ samples, it was found that the 2.50 mol% MnO doped $ZnO–V_2O_5–Nb_2O_5$ samples sintered at 900 °C is a candidate material for use in chip varistors.

The next chapter discusses about the effect of ZrO_2 doping on $ZnO–V_2O_5–Cr_2O_3$ based ceramics systems synthesized via solid state technique and sintered at 850, 900 & 950 °C on the structure and the influence of the grain boundary structure on the electrical properties of ZnO based ceramics in a systematic manner using AC impedance and dielectric spectroscopy (IS) have been analyzed.